



Article

Absorption and Emission Spectroscopic Investigation of the Thermal Dynamics of the Archaerhodopsin 3 Based Fluorescent Voltage Sensor QuasAr1

Alfons Penzkofer ^{1,*}, Arita Silapetere ² and Peter Hegemann ²

¹ Fakultät für Physik, Universität Regensburg, Universitätsstraße 31, D-93053 Regensburg, Germany

² Experimentelle Biophysik, Institut für Biologie, Humboldt Universität zu Berlin, Invalidenstraße 42, D-10115 Berlin, Germany

* Correspondence: alfons.penzkofer@physik.uni-regensburg.de; Tel.: +49-941-943-2107

Received: 21 July 2019; Accepted: 16 August 2019; Published: 21 August 2019



Abstract: QuasAr1 is a fluorescent voltage sensor derived from Archaerhodopsin 3 (Arch) of *Halorubrum sodomense* by directed evolution. Here we report absorption and emission spectroscopic studies of QuasAr1 in Tris buffer at pH 8. Absorption cross-section spectra, fluorescence quantum distributions, fluorescence quantum yields, and fluorescence excitation spectra were determined. The thermal stability of QuasAr1 was studied by long-time attenuation coefficient measurements at room temperature (23 ± 2 °C) and at 2.5 ± 0.5 °C. The apparent melting temperature was determined by stepwise sample heating up and cooling down (obtained apparent melting temperature: 65 ± 3 °C). In the protein melting process the originally present protonated retinal Schiff base (PRSB) with absorption maximum at 580 nm converted to de-protonated retinal Schiff base (RSB) with absorption maximum at 380 nm. Long-time storage of QuasAr1 at temperatures around 2.5 °C and around 23 °C caused gradual protonated retinal Schiff base isomer changes to other isomer conformations, de-protonation to retinal Schiff base isomers, and apoprotein structure changes showing up in ultraviolet absorption increase. Reaction coordinate schemes are presented for the thermal protonated retinal Schiff base isomerizations and deprotonations in parallel with the dynamic apoprotein restructurings.

Keywords: QuasArs; Archaerhodopsin 3; genetically encoded voltage sensors (GEVIs); absorption spectroscopic characterization; fluorescence spectroscopic characterization; apparent protein melting temperature; thermal stability; thermal isomerization; thermal deprotonation

1. Introduction

Changes in electrical potential across the plasma membrane of neurons are important for intercellular and intracellular signal transmission [1]. Classical electrophysiology techniques involve placing electrodes into biological tissue allowing to record membrane currents [2,3]. Optical recordings of membrane potential from cells, especially neurons, with fluorescent voltage sensitive dyes [4–8], genetically encoded calcium indicators (GECIs) [9–14], and with fluorescent genetically encoded voltage indicators (GEVIs) [15–28] is an active field of research. Two major groups of GEVIs are i) integral membrane voltage sensing domains (VSDs) composed of four trans-membrane helices fused to fluorescent proteins [15,17–20,25–27,29–34] and ii) microbial rhodopsins composed of 7 trans-membrane α -helices with covalently bound retinal isomers [14,16,25–27,35–38]. Generally microbial rhodopsins exhibit low fluorescence quantum yield in the range of $\phi_F = 2 \times 10^{-4}$ to 10^{-5} [39–41] which is too low for any cellular application. Directed evolution approach yielded modified microbial rhodopsins with increased fluorescence quantum yield, and few of them exhibited change of the fluorescence

intensity depending on the membrane voltage [14,15,25–27,35–38,42–48]. In rhodopsin-fluorescent protein GEVIs a microbial rhodopsin is fused with a highly fluorescent protein and the emission of the fused fluorescent protein changes upon membrane voltage changes [16,28,49,50].

Archaerhodopsin 3 (Arch) from *Halorubrum sodomense* with a single residue mutation D95N showed potential as a GEVI [36] and initiated the development of the Arch variants QuasAr1 and QuasAr2 (named according to ‘Quality superior to Arch’) [42]. QuasArs have improved fluorescence intensity and membrane voltage sensitivity [22,42,45]. The fluorescence quantum yield of wild-type Arch was reported to be $\phi_F = 9 \times 10^{-4}$ [36], of the mutant Arch D95N it was $\phi_F = 4 \times 10^{-4}$ [36,42], while for QuasAr1 it increased to $\phi_F = 8 \times 10^{-3}$ [42], and for QuasAr2 it was found to be $\phi_F = 4 \times 10^{-3}$ [42]. The lower fluorescence quantum yield of QuasAr2 compared to QuasAr1 is compensated by its higher voltage sensitivity [42]. QuasAr1 differs from the wild-type Arch by 5 mutations, namely P60S, T80S, D95H, D106H, and F161V [42]. The amino acid sequence of QuasAr1 is shown in Figure S1 of the Supplementary Materials (Section S1). Some structural formulae of retinal cofactors of rhodopsins are found in [51] and are shown in Figure S2 of the Supplementary Materials (Section S2). QuasAr2 differs from QuasAr1 by the counter ion mutation H95Q.

Here a detailed study is presented of the absorption and emission spectroscopic properties and the thermal dynamics of QuasAr1 in pH 8 Tris buffer. Aliquots of 30 μ L were used in the studies. They were stored at -80°C and thawed before usage. The absorption cross-section spectrum, excitation wavelength dependent fluorescence emission quantum distributions and quantum yields, and emission wavelength dependent fluorescence excitation spectra of purified QuasAr1 were determined. The thermal stability of QuasAr1 was studied by long-time spectroscopic studies at room temperature (21–25 $^\circ\text{C}$) and refrigerator temperature of $2.5 \pm 0.5^\circ\text{C}$. The apparent melting temperature was determined by stepwise sample heating up and cooling down. The temperature and time dependent retinal chromophore and opsin protein changes are discussed.

2. Results

2.1. Absorption and Emission Behavior of Fresh Thawed QuasAr1 Samples

The absorption coefficient spectrum $\alpha_a(\lambda)$ of a fresh thawed QuasAr1 sample was measured after centrifugation with 4400 rpm for 30 min at 4°C (Centrifuge 5702 R, Eppendorf AG, Hamburg, Germany). It is displayed by the solid curve in Figure 1. The main absorption band with maximum at wavelength $\lambda \approx 580$ nm is attributed to the singlet S_0 – S_1 transition of protonated retinal Schiff base (PRSB) and named Ret_580. The absorption in the range from 310 nm to 465 nm is thought to be comprised of singlet S_0 – S_n ($n \geq 2$) transitions of Ret_580 (dashed curve $\alpha_{a,\text{Ret}_580}(\lambda)$ in Figure 1, for its determination see section S3 of the Supplementary Materials) and singlet ground-state–excited-state transitions of residual retinal components (dotted curve $\alpha_{a,\text{residual retinals}}(\lambda) = \alpha_{a,\text{QuasAr1}}(\lambda) - \alpha_{a,\text{Ret}_580}(\lambda)$ in Figure 1). The short-wavelength absorption band peaking at $\lambda = 280$ nm is determined by apoprotein absorption (Trp, Tyr, Phe) and some retinal contribution.

The absorption cross-section spectrum of Ret_580, i.e., $\sigma_a(\lambda) = \alpha_{a,\text{Ret}_580}(\lambda) / N_{\text{Ret}_580}$ where N_{Ret_580} is the number density of Ret_580 chromophores in QuasAr1, is determined in section S3 of the Supplementary Materials (Figure S3).

Fluorescence emission quantum distributions $E_F(\lambda)$ of a fresh thawed QuasAr1 sample in pH 8 Tris buffer for fluorescence excitation wavelengths $\lambda_{F,\text{exc}}$ in the range from 260 nm to 640 nm are shown in Figure 2 and the corresponding fluorescence quantum yields are included in Figure 3 (see below). For $\lambda_{F,\text{exc}} > 500$ nm only S_1 – S_0 emission from Ret_580 is observed. The wavelength position of peak fluorescence emission is at $\lambda_{F,\text{max}} \approx 740$ nm. The full spectral half-width of this emission is $\delta\tilde{\nu}_{F,\text{Ret}_580} \approx 2900$ cm^{-1} . The Stokes shift is $\delta\tilde{\nu}_{\text{Stokes}} = \lambda_{a,\text{max}}^{-1} - \lambda_{F,\text{max}}^{-1} \approx 3730$ cm^{-1} . The strong Stokes shift and broad spectral width of the Ret_580 emission spectra indicate fluorescence emission along the S_1 excited state photo-isomerization path. Below it will be shown that Ret_580 is composed dominantly of two protonated retinal Schiff base isomers (Ret_580_I and Ret_580_{II}) in

different apoprotein conformations (Apoprotein_I and Apoprotein_{II}) which contribute to the broad fluorescence emission. In the Supplementary Materials (Table S1) wavelength positions of absorption maxima and fluorescence maxima together with Stokes shifts are listed for several rhodopsins (range of Stokes shifts from $\delta\tilde{\nu}_{Stokes} \approx 1750 \text{ cm}^{-1}$ for histidine kinase rhodopsin 1 from *Chlamydomonas reinhardtii* to $\delta\tilde{\nu}_{Stokes} \approx 4900 \text{ cm}^{-1}$ for proteorhodopsin from uncultivated marine γ -proteobacteria).

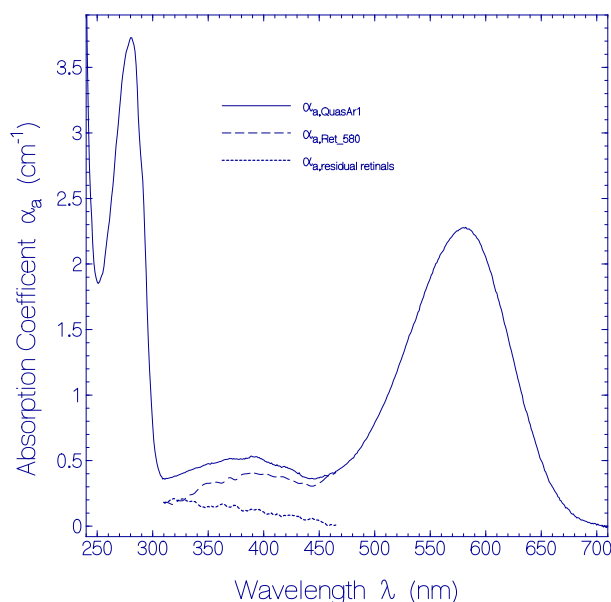


Figure 1. Absorption coefficient spectrum of a fresh thawed QuasAr1 sample in pH 8 Tris buffer. Solid curve: measured absorption coefficient spectrum $\alpha_{a,QuasAr1}(\lambda)$. Dashed curve: absorption coefficient spectrum $\alpha_{a,Ret_580}(\lambda)$ of PRSB Ret_580. Dotted curve: absorption coefficient spectrum of residual retinal components $\alpha_{a,residual\ retinals}(\lambda) = \alpha_{a,QuasAr1}(\lambda) - \alpha_{a,Ret_580}(\lambda)$.

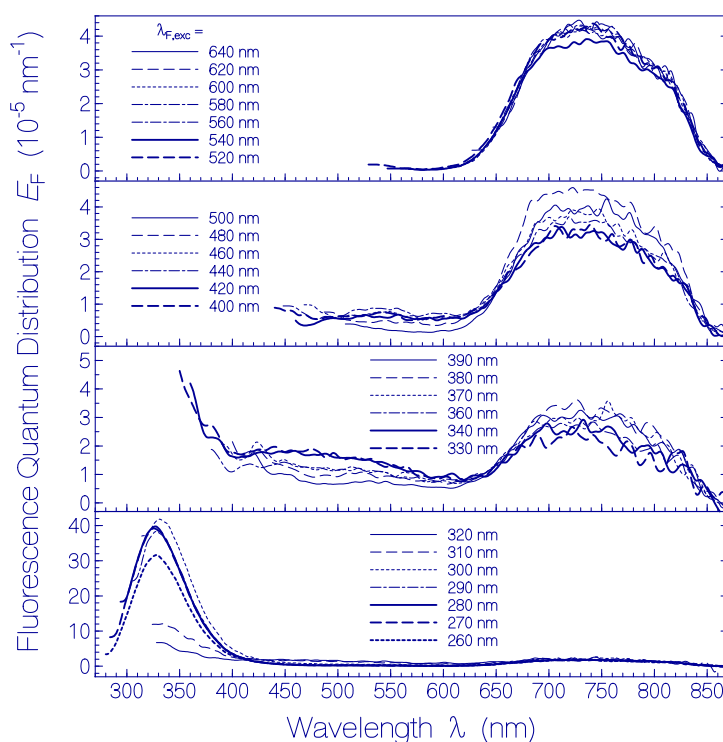


Figure 2. Fluorescence emission quantum distributions $E_F(\lambda)$ of fresh thawed QuasAr1 in pH 8 Tris buffer. The fluorescence excitation wavelengths $\lambda_{F,exc}$ are indicated in the sub-figures.

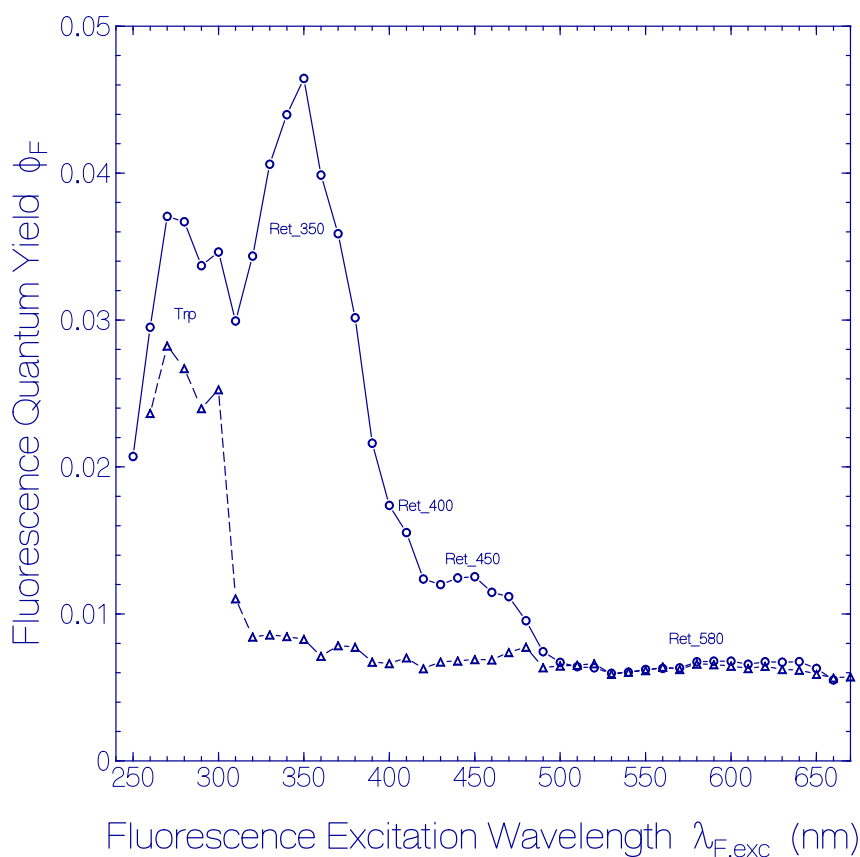


Figure 3. Dependence of the total fluorescence quantum yield ϕ_F on the fluorescence excitation wavelength $\lambda_{F,exc}$ for QuasAr1 in pH 8 Tris buffer. The dashed line connected triangles belong to a fresh thawed sample. The line-connected circles belong to a sample stored at 2.5 ± 0.5 °C in the dark over a period of 80 days.

Fluorescence excitation in the wavelength range from 400 nm to 480 nm indicates an additional fluorescence emission band around $\lambda_{F,max} \approx 550$ nm. It is thought to be caused by a small amount of a protonated retinal Schiff base isomer (named Ret_450, see below) absorbing in this range ($\delta\tilde{\nu}_{Stokes} \approx 4000$ cm^{-1}). Fluorescence excitation in the range from 330 nm to 390 nm resulted in a broad fluorescence emission band around $\lambda_{F,max} \approx 470$ nm. It is attributed to fluorescence emission of deprotonated retinal Schiff base isomer components. For fluorescence excitation in the wavelength region from 260 nm to 320 nm the fluorescence emission is dominated by Trp emission of the QuasAr1 apoprotein. The fluorescence emission maximum occurs at $\lambda_{F,max} = 328$ nm ($\delta\tilde{\nu}_{F,Trp} \approx 5600$ cm^{-1} , $\delta\tilde{\nu}_{Stokes} \approx 5200$ cm^{-1}). For all excitation wavelengths, the Ret_580 fluorescence emission band around $\lambda_{F,max} = 740$ nm is present since the Ret_580 absorption extends over the whole applied fluorescence excitation wavelength region due to S_0-S_n transitions ($n \geq 1$) with fast S_n-S_1 nonradiative relaxation for $n \geq 2$ and S_1-S_0 radiative emission. Additionally Förster-type energy transfer [52,53] occurs from Tyr and Trp to Ret_580 in the case of Tyr and Trp photo-excitation.

The dependence of the total fluorescence quantum yield $\phi_F = \int_{em} E_F(\lambda)d\lambda$ (the integration runs over the whole fluorescence emission wavelength region) of fresh thawed QuasAr1 on the fluorescence excitation wavelength $\lambda_{F,exc}$ is depicted by the dashed curve connected triangles in Figure 3. The fluorescence quantum yield is $\phi_F = (6.5 \pm 0.5) \times 10^{-3}$ for excitation in the wavelength region of S_0-S_1 absorption of Ret_580 ($\lambda_{F,exc} \geq 490$ nm). In the range of 380 nm $\leq \lambda_{F,exc} \leq 480$ nm it is $\phi_F = (7 \pm 0.5) \times 10^{-3}$, and in the range 320 nm $\leq \lambda_{F,exc} \leq 380$ nm it is $\phi_F = (8 \pm 0.5) \times 10^{-3}$ indicating a somewhat increased fluorescence efficiency of the additionally present retinal species besides Ret_580. In the range of 260 nm $\leq \lambda_{F,exc} \leq 310$ nm the fluorescence emission is dominated

by apoprotein Trp emission. There the fluorescence quantum yield increased to $\phi_F = 0.026 \pm 0.002$. The fluorescence emission of photo-excited Tyr is quenched by Förster-type energy transfer [52,53] to Trp (see supplementary material to [54]). The Trp fluorescence is reduced by Förster-type energy transfer [52,53] from Trp to the retinals in QuasAr1. The fluorescence quantum yields of Tyr and Trp in neutral water at 20 °C are $\phi_F(\text{Tyr}) = 0.14$ [55] and $\phi_F(\text{Trp}) = 0.15$ [56,57].

Normalized fluorescence excitation quantum distributions $E'_{ex}(\lambda)$ of a fresh thawed QuasAr1 sample in pH 8 Tris buffer for fluorescence detection wavelengths $\lambda_{F,det}$ in the range from 300 nm to 780 nm are shown in Figure S4 of the Supplementary Materials (section S4). They confirm the excitation wavelength dependent fluorescence emission of the dominant retinal component Ret_580 and other present retinal components.

2.2. Heating-Cooling Cycle of a Fresh Thawed QuasAr1 Sample

A fresh thawed sample of QuasAr1 was stepwise heated up to $\vartheta = 73.9$ °C, and then cooled down. Thereby attenuation coefficient spectra were measured. The results are shown in Figure 4. The applied temporal heating and cooling temperature profile is depicted in the right inset of Figure 4b. The apparent QuasAr1 protein melting temperature ϑ_m was determined by the onset of a steep attenuation rise in the transparency spectral region of QuasAr1 [58] due to coalescing of denatured unfolded proteins [59]. The apparent protein melting temperature is an indicator of the protein thermal stability.

The temperature dependent development of attenuation coefficient spectra $\alpha(\lambda)$ of QuasAr1 is shown in Figure 4a. Up to about 55 °C the attenuation spectra remained nearly unchanged (see top part of Figure 4a). Then the attenuation band of Ret_580 decreased and a new attenuation band around 380 nm built up (Ret_380). Light scattering became detectable above 55 °C and increased strongly above 65 °C. The temperature dependence of the light attenuation in the transparency region of QuasAr1 at 800 nm during the sample heating up is shown in the inset of the top part of Figure 4a. The apparent protein melting temperature determined by the onset of steeply rising light attenuation (light scattering) is $\vartheta_m = 65 \pm 3$ °C. The light scattering increased during heating up to 73.9 °C, and continued to increase during cooling down to 43.5 °C (see bottom part of Figure 4a). Then the light attenuation decreased likely due to aggregated particle sedimentation (see attenuation curve belonging to 31.5 °C in bottom part of Figure 4a). The final attenuation curve (dash-dotted curve in bottom part of Figure 4a) was obtained after centrifugation of the sample for 20 min with 4400 rpm at 4 °C.

The main part of Figure 4b shows the temperature dependent development of absorption coefficient spectra $\alpha_a(\lambda)$ of QuasAr1 during stepwise sample heating up (the attenuation coefficient spectra of Figure 4a were deprived of their scattering contribution, see procedure described in Section 4.2). The PRSB Ret_580 absorption band peaking around 580 nm decreased with rising temperature by deprotonation to RSB Ret_380 forming a new absorption band around 380 nm. For $\vartheta = 69.6$ °C Ret_580 is nearly completely converted to Ret_380. Therefore the curve $\alpha_a(\lambda, \vartheta = 69.6$ °C) in the wavelength range from ≈ 310 nm to ≈ 500 nm of Figure 4b represents the absorption coefficient spectrum of Ret_380. The absorption cross-section spectrum of Ret_380 is determined in section S3 of the Supplementary Materials from $\alpha_a(\lambda, \vartheta = 4$ °C) and $\alpha_a(\lambda, \vartheta = 69.6$ °C) of Figure 4b (dashed curve in Figure S3).

The left inset in Figure 4b displays the temperature dependent development of the absorption coefficients $\alpha_a(\vartheta)$ at $\lambda = 580$ nm (line-connected circles) and at $\lambda = 380$ nm (line-connected triangles). The curves clearly show the rising conversion of Ret_580 to Ret_380 with increasing temperature. The absorption at 380 nm below 40 °C is determined by the S_0 - S_n absorption of Ret_580 and the absorption of the already present deprotonated retinal Schiff base isomers of the fresh thawed unheated sample. In the stepwise sample heating the conversion of PRSB (Ret_580) to RSB (Ret_380) starts already at about $\vartheta = 40$ °C and becomes very strong above $\vartheta = 55$ °C well below the apparent protein melting temperature of $\vartheta_m \approx 65$ °C.

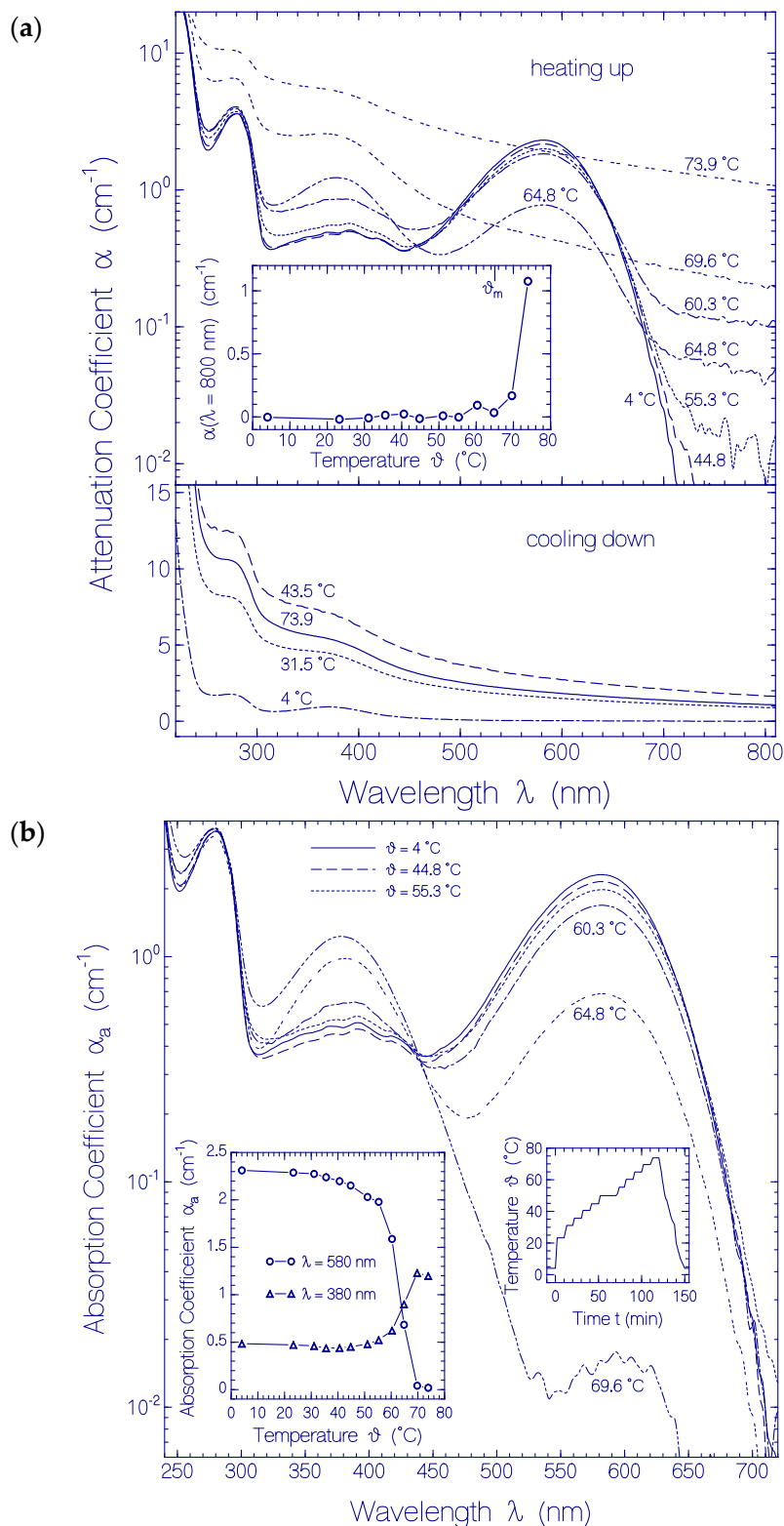


Figure 4. Heating-cooling cycle behavior of a fresh thawed QuasAr1 sample in pH 8 Tris buffer. (a) Attenuation coefficient spectra $\alpha(\lambda)$ development during stepwise sample heating up (top part) and cooling down (bottom part). Inset in top part: Temperature dependent attenuation coefficient development $\alpha(800 \text{ nm})$ during sample heating up. (b) Absorption coefficient spectra $\alpha_a(\lambda)$ development during stepwise sample heating up. Left inset: Temperature dependent absorption coefficient development $\alpha_a(580 \text{ nm})$ and $\alpha_a(380 \text{ nm})$. Right inset: Applied heating and cooling temperature profile $\vartheta(t)$.

2.3. Temporal Development of QuasAr1 at Refrigerator Temperature of 2.5 °C

The thermal stability of QuasAr1 in pH 8 Tris buffer at $\vartheta = 2.5 \pm 0.5$ °C in the dark was studied by carrying out transmission spectra measurements over a duration of 80 days and by measuring fluorescence emission and fluorescence excitation spectra at the end of the storage time.

The temporal development of the attenuation coefficient spectra $\alpha(\lambda)$ is shown in Figure 5. In the top main part attenuation coefficient spectra are shown for selected storage times t_{storage} . For $t_{\text{storage}} = 80$ days the attenuation spectra are shown before and after sample centrifugation to see the small light scattering contribution due to protein aggregation. The top inset shows the temporal attenuation coefficient development for some selected wavelengths. The bottom part displays difference attenuation spectra $\Delta\alpha(\lambda, t_{\text{storage}}) = \alpha(\lambda, t_{\text{storage}}) - \alpha(\lambda, 0) \left[\alpha(580 \text{ nm}, t_{\text{storage}}) / \alpha(580 \text{ nm}, 0) \right]$ for selected storage times.

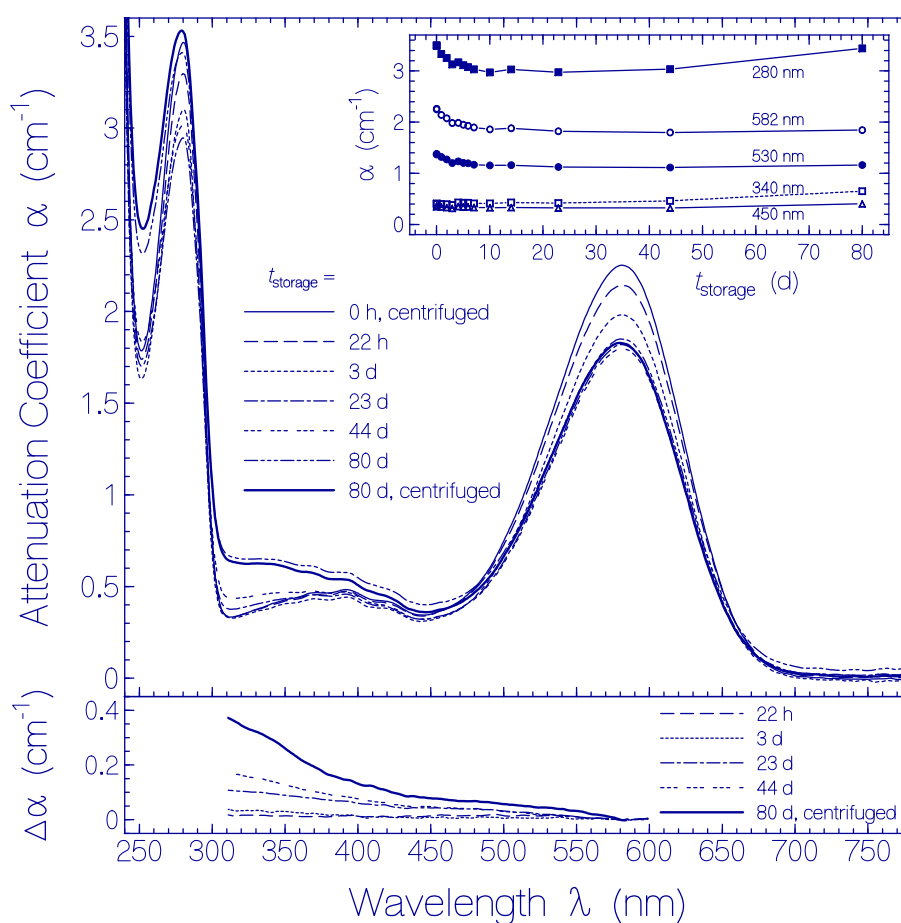


Figure 5. Temporal development of attenuation coefficient spectra $\alpha(\lambda, t_{\text{storage}})$ of QuasAr1 in pH 8 Tris buffer at 2.5 ± 0.5 °C in the dark. The storage times in the refrigerator are listed in the legend. The top inset shows attenuation coefficients at fixed wavelengths versus the storage time t_{storage} . The bottom part displays difference attenuation spectra $\Delta\alpha(\lambda, t_{\text{storage}}) = \alpha(\lambda, t_{\text{storage}}) - \alpha(\lambda, 0) \left[\alpha(580 \text{ nm}, t_{\text{storage}}) / \alpha(580 \text{ nm}, 0) \right]$.

Within the first ten days the attenuation coefficient of Ret_580 around 580 nm and the attenuation coefficient of the apoprotein around 280 nm decreased with time while the attenuation in the range from 310 nm to 470 nm remained approximately unchanged. The attenuation reduction around 580 nm and around 280 nm are attributed i) partly to the conversion of Ret_580 to other retinals absorbing in the 470–310 nm range (see differential attenuation coefficient spectra in the bottom part of Figure 5) and ii) partly to QuasAr1 tight small aggregate formation (specific surface reduction [60–62])

and/or loose aggregate cluster compactization with storage time (cluster size small therefore not showing up in light attenuation in the transparency spectral region; loosely packed globules with small volume fill factor densify to tightly packed globules, thereby the apparent absorption cross-section per molecule decreases because of specific surface reduction of the aggregates [63]). In the time range from $t_{\text{storage}} = 10$ d to 80 d the Ret_580 absorption band remained nearly unchanged. However, in this time range the apoprotein absorption changed. The main apoprotein absorption band around 280 nm increased and broadened (stronger absorption around 250 nm and around 310 nm). This behavior is attributed to dynamic QuasAr1 apoprotein restructuring. The increase of the apoprotein absorption strength is attributed to some increase of the oscillator strength of the S_0 to S_1 transition of Trp due to protein restructuring. In the wavelength range from 310 nm to 400 nm some absorption contribution from possibly formed dityrosine [64], tyrosinyl radicals [65], and tryptophanyl radicals [66] cannot be excluded [67]. The tryptophan involvement as chromophore element in photoreceptors is known for the UV-B photoreceptor UVR8 from *Arabidopsis thaliana* [68,69] (see also [51] with references therein) and for the LITE-1 photoreceptor in *Caenorhabditis elegans* [70,71].

Only a slight increase of light scattering was found after 80 days of storage by comparing the attenuation coefficient spectra measured before and after sample centrifugation (for 20 min at 4400 rpm). The slow spectral changes indicate the high thermal stability of QuasAr1 at 2.5 °C.

Fluorescence emission quantum distributions $E_F(\lambda)$ of QuasAr1 after 80 days of sample storage in the dark at 2.5 °C are shown in Figure 6. Fluorescence excitation in the wavelength range from $\lambda_{F,\text{exc}} = 500$ nm to 620 nm (top sub-figure) resulted in the fluorescence emission band of Ret_580 with fluorescence maximum around 740 nm. Sample excitation in the wavelength range from $\lambda_{F,\text{exc}} = 420$ nm to 480 nm (second top sub-figure) revealed a second fluorescence emission band with emission maximum around 540 nm. It is attributed to a PRSB isomer named Ret_450. In the second lowest sub-figure fluorescence emission spectra in the excitation wavelength region from $\lambda_{F,\text{exc}} = 320$ nm to 400 nm are displayed. A weak fluorescence band peaking around 470 nm is resolved for fluorescence excitation around $\lambda_{F,\text{exc}} \approx 400$ nm (RSB, Ret_400). A stronger fluorescence band peaking around 440 nm is observed for fluorescence excitation around $\lambda_{F,\text{exc}} \approx 350$ nm (RSB, Ret_350). A short-wavelength fluorescence band with maximum around 330 nm, in the bottom sub-figure of Figure 6, belongs to the apoprotein Trp emission (absorption band maximum around $\lambda_{F,\text{exc}} \approx 280$ nm). Fluorescence excitation in the wavelength range from $\lambda_{F,\text{exc}} = 240$ nm to 280 nm additionally caused fluorescence emission around 450 nm. This indicates excitation energy transfer from apoprotein absorbing species Tyr and Trp to Ret_350.

The excitation wavelength dependence of the total fluorescence quantum yield ϕ_F of QuasAr1 in pH 8 Tris buffer after 80 days of storage at 2.5 °C in the dark is displayed by the line-connected circle curve in Figure 3. The spectral changes of $\phi_F(\lambda_{F,\text{exc}})$ due to sample storage are seen easily by comparison with the $\phi_F(\lambda_{F,\text{exc}})$ curve a fresh thawed QuasAr1 sample (dashed-line connected triangle curve in Figure 3). For $\lambda_{F,\text{exc}} < 500$ nm the fluorescence quantum yield is increased by the thermally formed retinal isomers named Ret_450, Ret_400, and Ret_350 and by the thermally induced apoprotein restructuring with fluorescence emission of Trp ($\lambda_{F,\text{exc}}$ around 280 nm).

Normalized fluorescence excitation spectra of QuasAr1 in pH 8 Tris buffer stored in the dark at 2.5 °C for 80 days are presented in section S5 of the Supplementary Materials (Figure S5). They confirm the thermal formation of retinal isomers with increased fluorescence efficiency compared to Ret_580 and the Trp fluorescence emission.

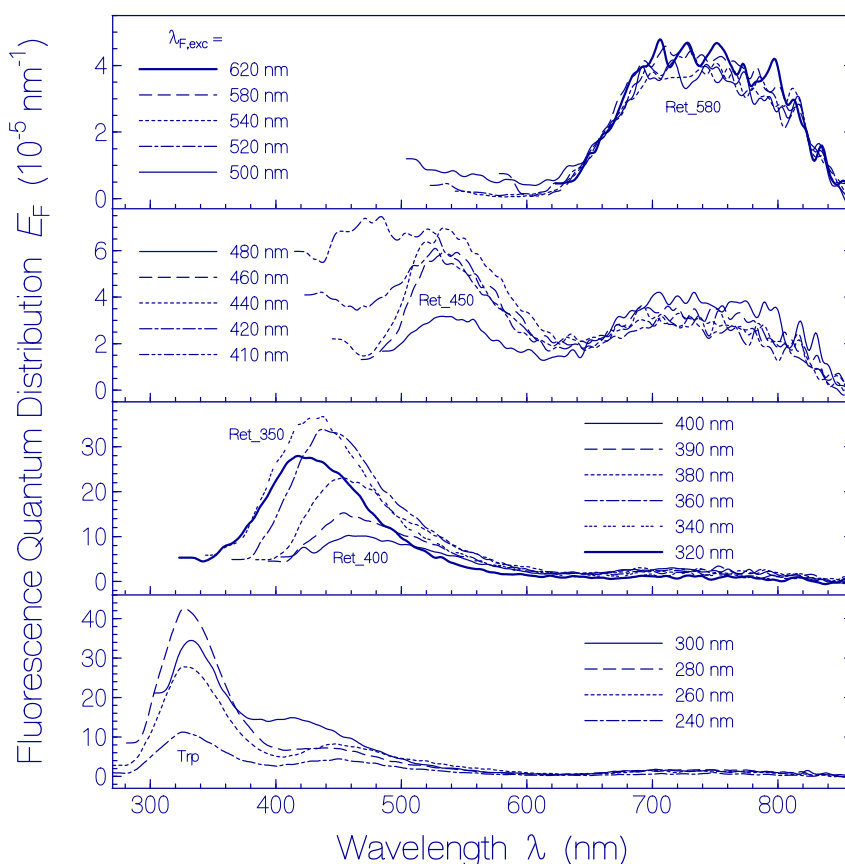


Figure 6. Fluorescence emission quantum distributions $E_F(\lambda)$ of QuasAr1 in pH 8 Tris buffer stored at 2.5 °C for a duration of 80 days. The fluorescence excitation wavelengths $\lambda_{F,exc}$ are listed in the legends.

2.4. Temporal Development of QuasAr1 at Room Temperature

The thermal stability of QuasAr1 in pH 8 Tris buffer at room temperature ($\vartheta = 21\text{--}25$ °C) in the dark was studied by carrying out transmission spectra measurements over a duration of 101 days and by measuring fluorescence emission and fluorescence excitation spectra after 50 days and at the end of the storage time.

The measured attenuation coefficient spectra $\alpha(\lambda)$ are presented in Figure S6 of the Supplementary Materials (Section S6). In Figure 7a the temporal development of the absorption coefficient spectra $\alpha_a(\lambda)$ is shown. The curves were derived from Figure S6 by removing the scattering contributions $\alpha_s(\lambda)$ according to $\alpha_a(\lambda) = \alpha(\lambda) - \alpha_s(\lambda)$ with $\alpha_s(\lambda) = \alpha_s(\lambda_0) \times (\lambda_0/\lambda)^\gamma$ whereby λ_0 was set to 800 nm and γ was adjusted in the transparency region (see below Section 4.2). The storage times are listed in the legend. The wavelength positions of maximum absorption of the originally present species (Ret_580 and Trp) and the formed species (Ret_530, Ret_500, Ret_450, Ret_400, Ret_350) are indicated.

In the main part of Figure 7a it is seen that the absorption decreased around 580 nm (PRSB, Ret_580), and new absorption built-up and decreased around 500 nm (PRSB, Ret_500). The absorption increased with storage time around 400 nm (RSB, Ret_400) and around 350 nm (RSB, Ret_350). The temporal increase of absorption below 320 nm is attributed to apoprotein restructuring with Trp enlarged absorption oscillator strength.

The inset of Figure 7a shows the dependence of the absorption coefficient $\alpha_a(580\text{ nm})$ versus storage time $t_{storage}$ (circles are experimental data). The decrease of the absorption coefficient with storage time is fitted by a two-component single exponential decay function according to:

$$\alpha_{a,580\text{ nm}}(t_{storage}) = \alpha_{a,580\text{ nm}}(0) \left[\kappa_{Ret_{580,I}} \exp(-t_{storage}/\tau_{Ret_{580,I}}) + \kappa_{Ret_{580,II}} \exp(-t_{storage}/\tau_{Ret_{580,II}}) \right] \quad (1)$$

In Equation (1) $\alpha_{a,580\text{ nm}}(0)$ is the total initial absorption coefficient at $t_{\text{storage}} = 0$. $\kappa_{\text{Ret}_{580\text{I}}}$ is the fraction of Ret_580 with fast absorption decay time constant $\tau_{\text{Ret}_{580\text{I}}}$. This component is named Ret_580_I. $\kappa_{\text{Ret}_{580\text{II}}} = 1 - \kappa_{\text{Ret}_{580\text{I}}}$ is the fraction of Ret_580 with slow absorption decay time constant $\tau_{\text{Ret}_{580\text{II}}}$. This component is named Ret_580_{II}. The fit parameters are $\alpha_{a,580\text{ nm}}(0) = 2.193\text{ cm}^{-1}$, $\kappa_{\text{Ret}_{580\text{I}}} = 0.41$, $\tau_{\text{Ret}_{580\text{I}}} = 3.8\text{ d}$, $\kappa_{\text{Ret}_{580\text{II}}} = 0.59$, and $\tau_{\text{Ret}_{580\text{II}}} = 120\text{ d}$.

In Figure 7b the temporal development of absorption coefficient spectra of new formed species (Ret_640, Ret_530, Ret_500, Ret_450, Ret_400, Ret_350) are displayed. In the main part of Figure 7b the Ret_580 contribution $\alpha_{a,\text{Ret}_{580}}(\lambda, t_{\text{storage}})$ and the original residual retinal contributions $\alpha_{a,\text{residual retinals}}(\lambda)$ are subtracted from $\alpha_a(\lambda, t_{\text{storage}})$ of Figure 7a, i.e.:

$$\Delta\alpha_a(\lambda, t_{\text{storage}}) = \alpha_a(\lambda, t_{\text{storage}}) - \alpha_{a,\text{Ret}_{580}}(\lambda, t_{\text{storage}}) - \alpha_{a,\text{residual retinals}}(\lambda, 0) \quad (2)$$

is displayed. The curves show i) formation of a weak absorption band around 640 nm (formation of PRSB isomer Ret_640), ii) build-up and decrease of a broad absorption band around 500 nm (formation of PRSB Ret_500), iii) build-up of an absorption band around 400 nm (formation of RSB isomer Ret_400), iv) build-up of an absorption band around 350 nm (formation of RSB isomer Ret_350), and v) build-up of long-wavelength apoprotein absorption in the range $< 340\text{ nm}$. The Ret_500 absorption band changed its shape for long-time sample storage $t_{\text{storage}} \geq 50\text{ d}$. Shoulders are seen around $\lambda \approx 530\text{ nm}$ (Ret_530) and around $\lambda \approx 450\text{ nm}$ (Ret_450). They may be due to new formed retinal isomer forms or due to Ret_500 isomer position shift due to apoprotein adjacent structure changes. The minor part of the PRSB isomer Ret_580 (fraction $\kappa_{\text{Ret}_{580\text{I}}}$, named Ret_580_I, likely a *cis* isomer) is converted dominantly to the short wavelength absorbing PRSB Ret_500 (likely a *trans* isomer), and the dominant part of the PRSB isomer Ret_580 (fraction $\kappa_{\text{Ret}_{580\text{II}}}$, named Ret_580_{II}, likely a *trans* isomer) is converted to the long-wavelength absorbing PRSB isomer Ret_640 (likely a *cis* isomer). Ret_500 is thought to deprotonate to Ret_400 (likely a RSB *trans* isomer), and Ret_640 is thought to deprotonate to Ret_350 (likely a RSB *cis* isomer).

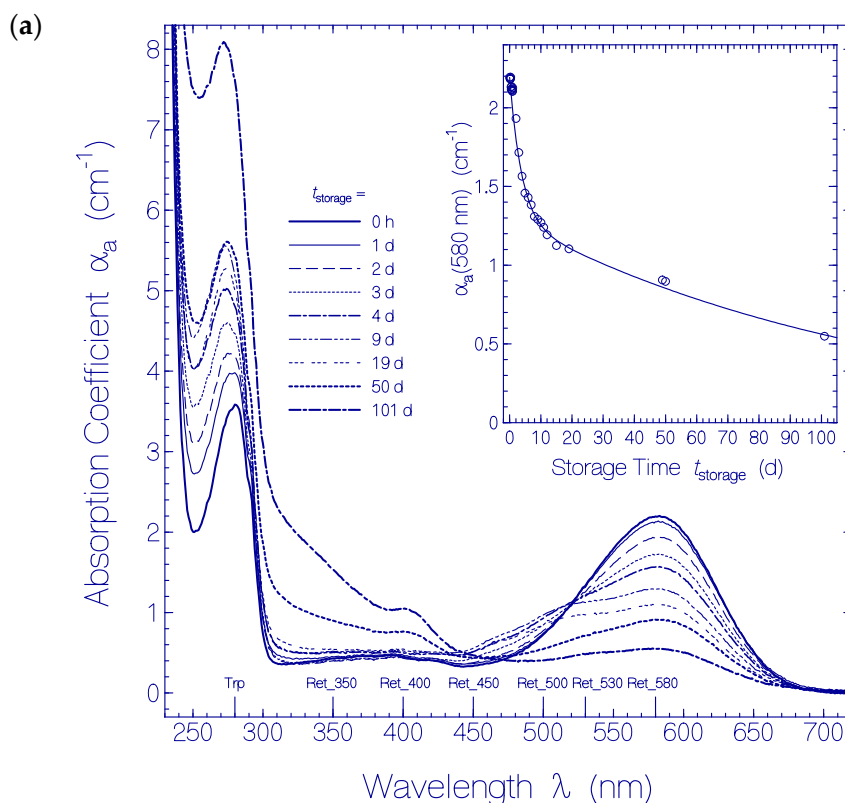


Figure 7. Cont.

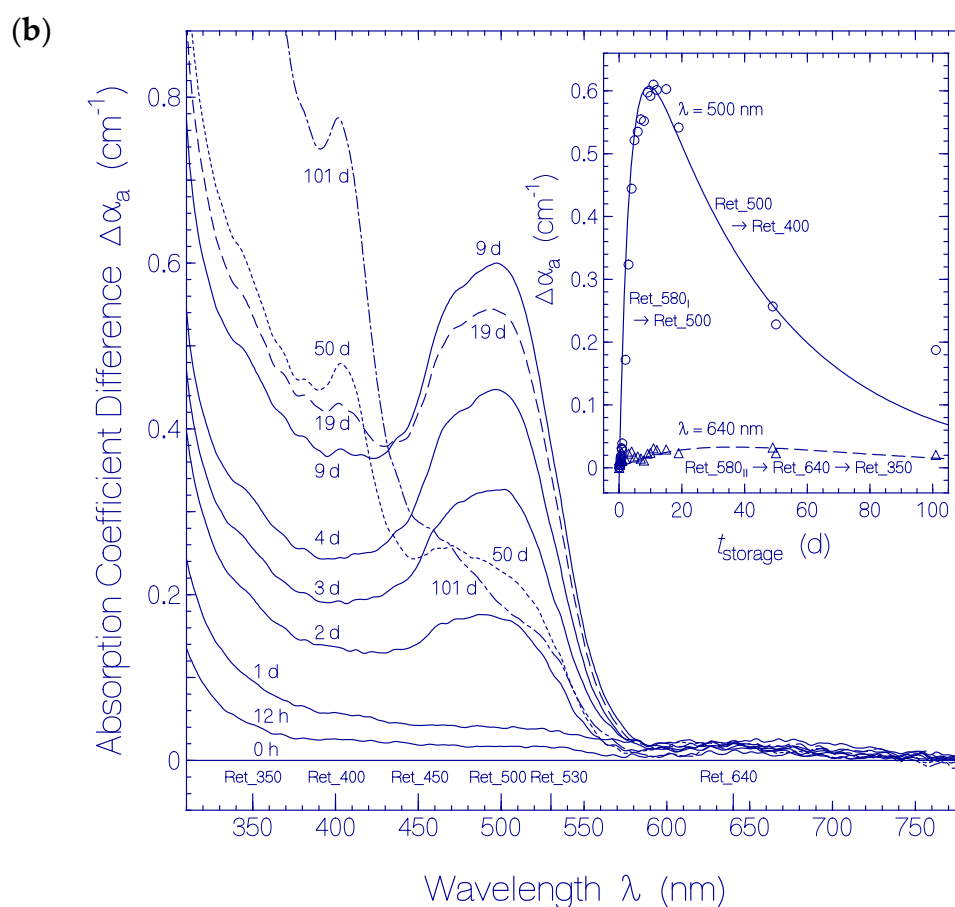


Figure 7. (a) Temporal development of absorption coefficient spectra $\alpha_a(\lambda)$ of QuasAr1 in pH 8 Tris buffer stored in the dark at room temperature ($\vartheta = 21\text{--}25\text{ }^\circ\text{C}$). The storage times are listed in the legend ($t_{\text{storage}} = 0\text{ h}$ refers to absorption coefficient spectrum measurement immediately after sample thawing). The inset shows the temporal development of $\alpha_a(580\text{ nm})$ where the circles are data points and the solid curve is a two-component single exponential fit according to $\alpha_{a,580\text{ nm}}(t_{\text{storage}}) = \alpha_{a,580\text{ nm}}(0) [\kappa_{\text{Ret}_{580\text{I}}} \exp(-t_{\text{storage}}/\tau_{\text{Ret}_{580\text{I}}}) + \kappa_{\text{Ret}_{580\text{II}}} \exp(-t_{\text{storage}}/\tau_{\text{Ret}_{580\text{II}}})]$ with $\alpha_{a,580\text{ nm}}(0) = 2.193\text{ cm}^{-1}$, $\kappa_{\text{Ret}_{580\text{I}}} = 0.41$, $\tau_{\text{Ret}_{580\text{I}}} = 3.8\text{ d}$, $\kappa_{\text{Ret}_{580\text{II}}} = 0.59$, and $\tau_{\text{Ret}_{580\text{II}}} = 120\text{ d}$. (b) Temporal development of the corresponding difference absorption coefficient spectra $\Delta\alpha_a(\lambda, t_{\text{storage}}) = \alpha_a(\lambda, t_{\text{storage}}) - \alpha_{a,\text{Ret}_{580}}(\lambda, t_{\text{storage}}) - \alpha_{a,\text{residual retinals}}(\lambda, 0)$. The inset shows $\Delta\alpha_a$ at $\lambda = 500\text{ nm}$ and $\lambda = 640\text{ nm}$ versus storage time t_{storage} . The $\Delta\alpha_a$ data at $\lambda = 500\text{ nm}$ are fitted by $\Delta\alpha_{a,500\text{ nm}}(t_{\text{storage}}) = \Delta\alpha_{a,500\text{ nm,max}} [1 - \exp(-t_{\text{storage}}/\tau_{\text{Ret}_{580\text{I}}})] \exp(-t_{\text{storage}}/\tau_{\text{PT,I}})$ with $\Delta\alpha_{a,500\text{ nm,max}} = 0.83\text{ cm}^{-1}$, $\tau_{\text{Ret}_{580\text{I}}} = 3.8\text{ d}$, and $\tau_{\text{PT,I}} = 42\text{ d}$. The $\Delta\alpha_a$ data at $\lambda = 640\text{ nm}$ are fitted by $\Delta\alpha_{a,640\text{ nm}}(t_{\text{storage}}) = \Delta\alpha_{a,640\text{ nm,max}} [1 - \exp(-t_{\text{storage}}/\tau_{\text{Ret}_{580\text{II}}})] \exp(-t_{\text{storage}}/\tau_{\text{PT,II}})$ with $\Delta\alpha_{a,640\text{ nm,max}} = 0.3\text{ cm}^{-1}$, $\tau_{\text{Ret}_{580\text{II}}} = 120\text{ d}$, and $\tau_{\text{PT,II}} = 42\text{ d}$.

The inset in Figure 7b displays the temporal development of $\Delta\alpha_a(500\text{ nm})$ (circles, initial build-up of Ret_500 due to conversion of Ret_580_I to Ret_500 and subsequent decrease of Ret_500 due to conversion to Ret_400) and the temporal development of $\Delta\alpha_a(640\text{ nm})$ (triangles, weak build-up of Ret_640 due to conversion of Ret_580_{II} to Ret_640 and concurrent conversion of Ret_640 to Ret_350). The temporal development of $\Delta\alpha_a(500\text{ nm})$ is fitted by:

$$\Delta\alpha_{a,500\text{ nm}}(t_{\text{storage}}) = \Delta\alpha_{a,500\text{ nm,max}} [1 - \exp(-t_{\text{storage}}/\tau_{\text{Ret}_{580\text{I}}})] \exp(-t_{\text{storage}}/\tau_{\text{PT,I}}) \quad (3)$$

$\Delta\alpha_{a,500\text{ nm,max}}$ is the expected maximum $\Delta\alpha_a(500\text{ nm})$ for $t_{\text{storage}} \rightarrow \infty$ in the absence of deprotonation ($\tau_{\text{PT,I}} \rightarrow \infty$). $\tau_{\text{Ret}_{580\text{I}}}$ is the decay time constant of Ret_580_I. $\tau_{\text{PT,I}}$ is the time constant of Ret_500

deprotonation. The fit parameters are $\Delta\alpha_{a,500\text{ nm,max}} = 0.83\text{ cm}^{-1}$, $\tau_{\text{Ret}_{580\text{I}}} = 3.8\text{ d}$, and $\tau_{\text{PT,II}} = 42\text{ d}$. ($\Delta\alpha_{a,500\text{ nm}}$ at $t_{\text{storage}} = 101\text{ d}$ is larger than the fit value since short-wavelength absorption bands extend to $\lambda = 500\text{ nm}$ and $\Delta\alpha_{a,500\text{ nm}}(101\text{ d})$ is not only due to Ret_{500} absorption).

The temporal development of $\Delta\alpha_a(640\text{ nm})$ is fitted by:

$$\Delta\alpha_{a,640\text{ nm}}(t_{\text{storage}}) = \Delta\alpha_{a,640\text{ nm,max}} \left[1 - \exp(-t_{\text{storage}}/\tau_{\text{Ret}_{580\text{II}}}) \right] \exp(-t_{\text{storage}}/\tau_{\text{PT,II}}) \quad (4)$$

$\Delta\alpha_{a,640\text{ nm,max}}$ is the expected maximum $\Delta\alpha_a(640\text{ nm})$ for $t_{\text{storage}} \rightarrow \infty$ in the absence of deprotonation ($\tau_{\text{PT,II}} \rightarrow \infty$). $\tau_{\text{Ret}_{580\text{II}}}$ is the decay time constant of $\text{Ret}_{580\text{II}}$. $\tau_{\text{PT,II}}$ is the time constant of Ret_{640} deprotonation. The fit parameters are $\Delta\alpha_{a,640\text{ nm,max}} = 0.3\text{ cm}^{-1}$, $\tau_{\text{Ret}_{580\text{II}}} = 120\text{ d}$, and $\tau_{\text{PT,II}} = 42\text{ d}$.

Fluorescence emission quantum distributions $E_F(\lambda)$ of QuasAr1 after 50 days of sample storage in the dark at room temperature ($\vartheta = 21\text{--}25\text{ }^\circ\text{C}$) are shown in Figure 8. Fluorescence excitation in the wavelength range of $\lambda_{\text{F,exc}} \geq 560\text{ nm}$ (top sub-figure) resulted in the fluorescence emission band of Ret_{580} with fluorescence maximum around 740 nm . Sample excitation in the region from $\lambda_{\text{F,exc}} = 540\text{ nm}$ to $\lambda_{\text{F,exc}} = 420\text{ nm}$ (second top sub-figure) resulted in peak fluorescence emission in the range from 550 nm to 530 nm . This emission is dominantly attributed to the formed protonated retinal Schiff base isomers Ret_{530} , Ret_{500} , and Ret_{450} . In the second lowest sub-figure fluorescence emission spectra are resolved resulting from the deprotonated retinal Schiff base isomers Ret_{400} ($\lambda_{\text{F,exc}} \approx 400\text{ nm}$, $\lambda_{\text{F,max}} \approx 470\text{ nm}$, weak fluorescence emission) and Ret_{350} ($\lambda_{\text{F,exc}} \approx 350\text{ nm}$, $\lambda_{\text{F,max}} \approx 430\text{ nm}$). In the bottom sub-figure the fluorescence emission peaking around $\lambda_{\text{F,max}} \approx 330\text{ nm}$ is due to the apoprotein Trp emission (either directly excited or populated by excitation transfer from photo-excited Tyr to Trp).

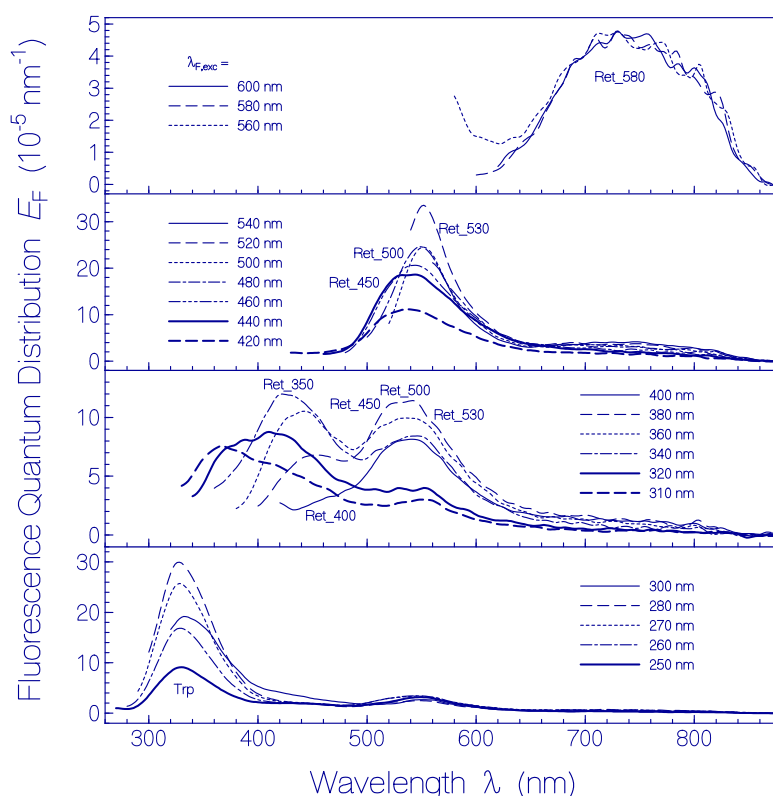


Figure 8. Fluorescence emission quantum distributions $E_F(\lambda)$ of QuasAr1 in pH 8 Tris buffer stored at room temperature ($\vartheta = 21\text{--}25\text{ }^\circ\text{C}$) for a duration of 50 days. The fluorescence excitation wavelengths $\lambda_{\text{F,exc}}$ are listed in the legends.

In Figure S7 of the Supplementary Materials (Section S7) the fluorescence emission quantum distributions of QuasAr1 after 101 days of storage in the dark at room temperature are shown. The reduced presence of weakly fluorescing Ret_580 increased the overall fluorescence quantum yield in the wavelength region from 420 nm to 540 nm (stronger fluorescent Ret_530 and Ret_450).

The excitation wavelength dependence of the fluorescence quantum yield ϕ_F of QuasAr1 in pH 8 Tris buffer after 50 days and after 101 days of storage in the dark at room temperature is displayed in Figure 9. ϕ_F is the ratio of the total amount of emitted fluorescence photons to the total amount of absorbed photons from the various absorbing species i in QuasAr1 at the selected excitation wavelength $\lambda_{F,exc}$. This means:

$$\phi_F(\lambda_{F,exc}) = \sum_i \frac{\alpha_{a,i}(\lambda_{F,exc})}{\alpha_a(\lambda_{F,exc})} \phi_{F,i}(\lambda_{F,exc}) \quad (5)$$

where i runs over the species absorbing at $\lambda_{F,exc}$ with the absorption coefficients $\alpha_{a,i}(\lambda_{F,exc})$, $\phi_{F,i}(\lambda_{F,exc})$ is the fluorescence quantum yield of component i , and $\alpha_a(\lambda_{F,exc}) = \sum_i \alpha_{a,i}(\lambda_{F,exc})$ is the total absorption coefficient at $\lambda_{F,exc}$. The wavelength positions of the absorption band maxima of the present components, protonated retinal Schiff bases Ret_580, Ret_530, Ret_500, Ret_450, deprotonated retinal Schiff bases Ret_400 and Ret_350, and the apoprotein contribution Trp are indicated at the bottom of Figure 9. The fluorescence quantum yield contributions of Ret_500 and Ret_400 are not well resolved. The fluorescence quantum yield of Ret_580 of $\phi_F \approx 0.007$ is the same after 50 days and 101 days of storage as of the fresh sample immediately after thawing. Ret_530, Ret_450, and Ret_350 are a factor of 5 to 10 stronger fluorescent than Ret_580. The fluorescence quantum yield of the apoprotein $\phi_{F,Trp}$ is reduced by apoprotein excitation energy transfer to the retinal isomers.

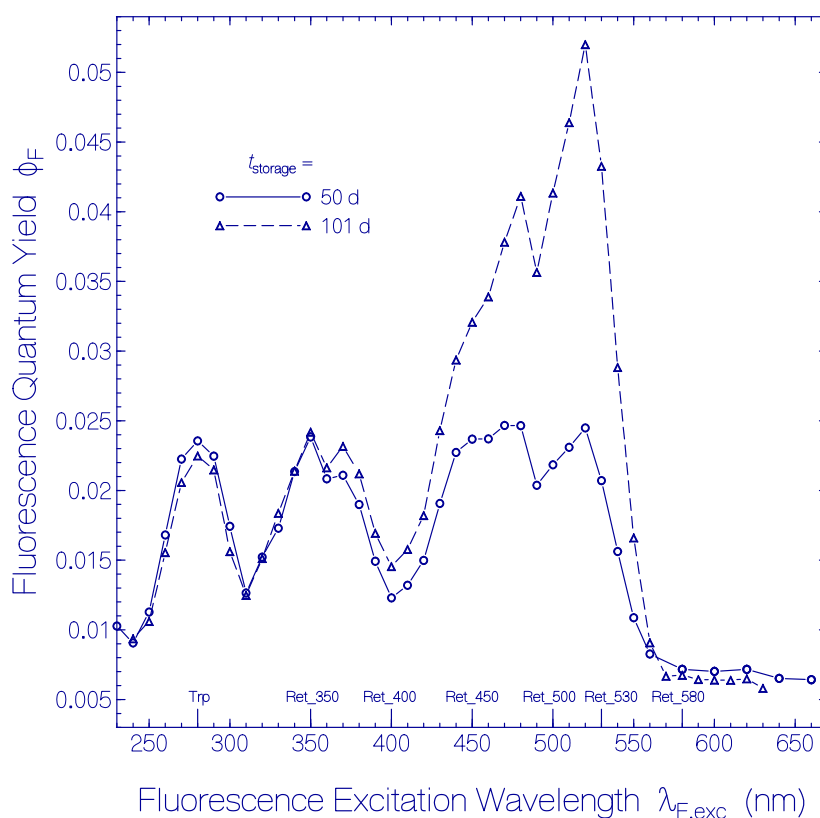


Figure 9. Dependence of the total fluorescence quantum yield ϕ_F on fluorescence excitation wavelength $\lambda_{F,exc}$ for QuasAr1 in pH 8 Tris buffer stored in the dark at room temperature ($\vartheta = 21\text{--}25\text{ }^\circ\text{C}$) for durations of 50 days and 101 days.

Normalized fluorescence excitation spectra of QuasAr1 in pH 8 Tris buffer stored in the dark at room temperature for 50 days (Figure S8) and 101 days (Figure S9) are presented in section S8 of the Supplementary Materials. They confirm the thermal formation of retinal isomers with increased fluorescence efficiency compared to Ret_580 and the thermal apoprotein restructuring with increased absorption strength. The formation of small amounts of strongly fluorescent protonated retinal Schiff base isomers Ret_530 and Ret_450 by thermal activated ground-state isomerization of Ret_580 are resolved in Figures S8 and S9.

3. Discussion

In Section 2 we reported spectroscopic investigation of QuasAr1 absorption and emission at pH 8 in Tris buffer. The samples were studied under different conditions: i) fresh thawed samples, ii) thermally aged samples at refrigerated temperature (2.5 °C) and room temperature (21–25 °C), and iii) heat-denatured samples. The measurements provided information on the thermal protein stability, the presence of different original apoprotein structures, the original retinal isomer composition, the thermal induced isomer conformation changes, the protonated retinal Schiff base isomers (PRSB) proton release to deprotonated retinal Schiff base isomers (RSB), and the thermal apoprotein restructuring of the originally present apoprotein structures showing up in UV spectral changes and absorption strength increase. The formation of new protonated retinal Schiff base isomers and their deprotonation to retinal Schiff base isomers occurred in parallel with the dynamic opsin apoprotein restructuring.

In the heterologous expression of QuasAr1 the retinal cofactor is covalently bound to the opsin protein via a lysine Schiff base. It is dominantly present in protonated form. About 86% of retinal was found to be present as protonated retinal Schiff base (PRSB) Ret_580, and about 14% were found to be present mainly as neutral retinal Schiff base (RSB) isomers Ret_400 and Ret_350 and small amounts of other protonated retinal Schiff base isomers as Ret_450 (see Figure 1 and section S4 of the Supplementary Materials).

At refrigerator temperature (≈ 2.5 °C) over a period of 80 days only small conversion of Ret_580 to Ret_500, Ret_450, Ret_400 and Ret_350 was observed. Some apoprotein restructuring showed up in increased UV absorption strength.

At room temperature (≈ 23 °C) within the observation time of 101 days formation of new PRSB isomers (Ret_640, Ret_530, Ret_500, Ret_450) and significant deprotonation of the PRSB isomers to RSB isomers (Ret_640 to Ret_350, Ret_500 to Ret_400) occurred together with apoprotein restructuring showing up in increased UV absorption. The temporal two-component single exponential absorption decrease of Ret_580 (Figure 7a) indicated its composition of two main isomer components Ret_580_I (likely a PRSB *cis* isomer in a specific QuasAr1 amino acid residue arrangement Apoprotein_{initial,I}) and Ret_580_{II} (likely a PRSB *trans* isomer in another specific QuasAr1 amino acid residue arrangement Apoprotein_{initial,II}). The temporal formation and decay of the absorption coefficient spectra of new formed species (Figure 7b) indicated i) a ground-state thermal activated isomerization of Ret_580_I to Ret_500 (likely a PRSB *trans* isomer) and the subsequent deprotonation of Ret_500 to Ret_400 (likely a RSB *trans* isomer), and ii) a ground-state thermal activated isomerization of Ret_580_{II} to Ret_640 (likely a PRSB *cis* isomer) and the concurrent deprotonation of Ret_640 to Ret_350 (likely a RSB *cis* isomer). QuasAr1 sample heating above 60 °C resulted in fast PRSB chromophore deprotonation to RSB. The thermal studies indicated energy barrier involved ground-state isomerizations, irreversible protein restructuring with irreversible protonated retinal Schiff base deprotonation and intrinsic apoprotein residue (mainly Trp) rearrangement with increased absorption oscillator strength.

The protonated retinal Schiff base ground-state isomerization, protonated retinal Schiff base deprotonation, and the apoprotein restructuring dynamics are illustrated in Figure 10. The top part illustrates the isomerization of the PRSB Ret_580_{II} isomer (likely all-*trans* isomer in a specific QuasAr1 protein conformation Apoprotein_{II}) to the PRSB Ret_640 isomer (likely 13-*cis* isomer in the same specific QuasAr1 protein conformation) and the concurrent proton release from Ret_640 to the stable formation of Ret_350 (likely a RSB 13-*cis* isomer). The middle part illustrates the isomerization of the PRSB

Ret_{580_I} isomer (likely 13-*cis* isomer in a specific QuasAr1 protein conformation Apoprotein_I) to the PRSB Ret₅₀₀ isomer (likely all-*trans* isomer in the same specific QuasAr1 protein conformation) and the subsequent proton release from Ret₅₀₀ to the stable formation of Ret₄₀₀ (likely a RSB all-*trans* isomer). The bottom part illustrates the concurrent occurring apoprotein restructuring supporting the ground-state protonated retinal Schiff base isomerizations and deprotonations.

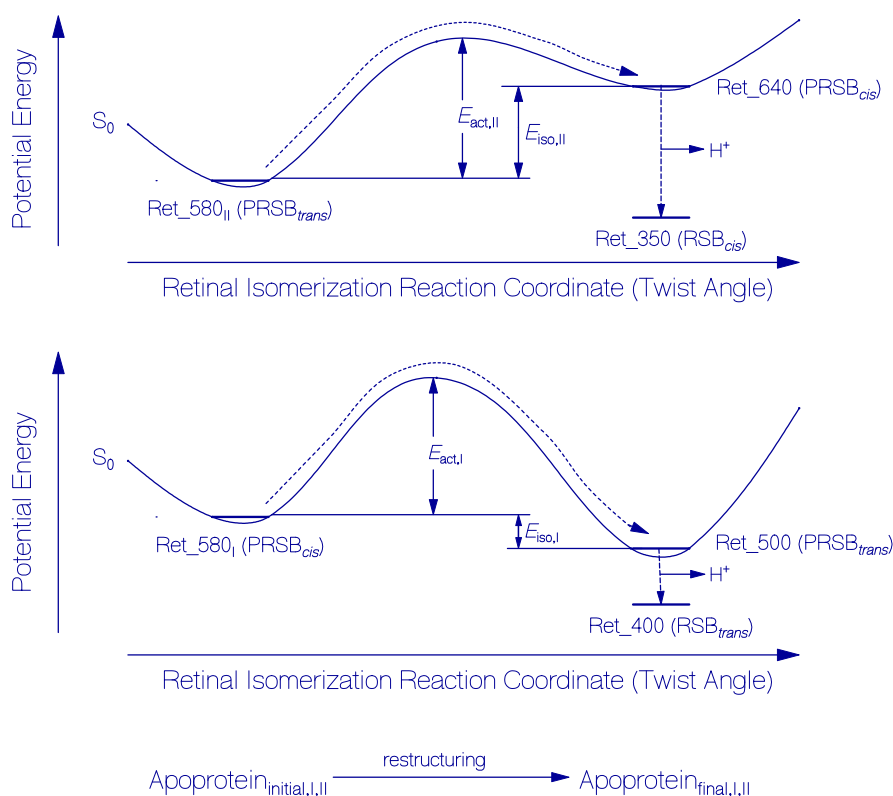


Figure 10. Schematic reaction coordinate diagrams for thermal activated S_0 ground-state protonated retinal Schiff base isomerizations and apoprotein restructuring assisted irreversible deprotonations to retinal Schiff base isomers. Top part: Isomerization of Ret_{580_{II}} to Ret₆₄₀ and subsequent deprotonation to Ret₃₅₀. Middle part: Isomerization of Ret_{580_I} to Ret₅₀₀ and subsequent deprotonation to Ret₄₀₀. Bottom part: Parallel occurring opsin restructuring of originally present apoprotein structures (Apoprotein_{initial,I} and Apoprotein_{initial,II}) to final apoprotein structures (Apoprotein_{final,I} and Apoprotein_{final,II}) of QuasAr1 acting on protonated retinal Schiff base isomerization and deprotonation.

The energetic level positions $E_{iso,I}$ of Ret₅₀₀ and $E_{iso,II}$ of Ret₆₄₀ may be estimated from the expected maximum absorption differences $\Delta\alpha_{a,500\text{ nm,max}}$ and $\Delta\alpha_{a,640\text{ nm,max}}$ of Equations (3) and (4). Assuming equal absorption cross-sections $\sigma_{a,\text{Ret}_{580}}(580\text{ nm})$, $\sigma_{a,\text{Ret}_{500}}(500\text{ nm})$, and $\sigma_{a,\text{Ret}_{640}}(640\text{ nm})$, the fractions $\chi_{\text{Ret}_{500}}$ and $\chi_{\text{Ret}_{640}}$ of thermally populated Ret₅₀₀ and Ret₆₄₀ would be [54]:

$$\chi_{\text{Ret}_{500}} = \frac{\Delta\alpha_{a,500\text{ nm,max}}}{\alpha_{a,580\text{ nm}}(0)\kappa_{\text{Ret}_{580,I}}} \quad (6)$$

$$\chi_{\text{Ret}_{640}} = \frac{\Delta\alpha_{a,640\text{ nm,max}}}{\alpha_{a,580\text{ nm}}(0)\kappa_{\text{Ret}_{580,II}}} \quad (7)$$

The energy level positions $E_{iso,I}$ and $E_{iso,II}$ are obtained by application of the Boltzmann level position law [72]:

$$\chi_{\text{Ret}_{500}} = \frac{\exp(-E_{iso,I}/(k_B\vartheta))}{1 + \exp(-E_{iso,I}/(k_B\vartheta))} \quad (8)$$

and:

$$\chi_{\text{Ret}_640} = \frac{\exp(-E_{\text{iso},II}/(k_B\vartheta))}{1 + \exp(-E_{\text{iso},II}/(k_B\vartheta))} \quad (9)$$

where k_B is the Boltzmann constant and ϑ is the temperature.

Solving Equations (8) and (9) for $E_{\text{iso},I}$ and $E_{\text{iso},II}$ gives:

$$E_{\text{iso},I} = -\ln\left(\frac{\chi_{\text{Ret}_500}}{1 - \chi_{\text{Ret}_500}}\right)k_B\vartheta \quad (10)$$

and:

$$E_{\text{iso},II} = -\ln\left(\frac{\chi_{\text{Ret}_640}}{1 - \chi_{\text{Ret}_640}}\right)k_B\vartheta \quad (11)$$

Insertion of parameters gives: $\chi_{\text{Ret}_500} = 0.92$ ($\Delta\alpha_{a,500 \text{ nm,max}} = 0.83 \text{ cm}^{-1}$, $\alpha_{a,580 \text{ nm}}(0) = 2.193 \text{ cm}^{-1}$, $\kappa_{\text{Ret}_580,I} = 0.41$), $\chi_{\text{Ret}_640} = 0.23$ ($\Delta\alpha_{a,500 \text{ nm,max}} = 0.3 \text{ cm}^{-1}$, $\alpha_{a,580 \text{ nm}}(0) = 2.193 \text{ cm}^{-1}$, $\kappa_{\text{Ret}_580,II} = 0.59$), $E_{\text{iso},I} = -9.98 \times 10^{-21} \text{ J} = -500 \text{ cm}^{-1} \times hc_0$ ($k_B = 1.38 \times 10^{-23} \text{ J K}^{-1}$, $\vartheta = 296 \text{ K}$ is temperature, h is the Planck constant, and c_0 is the speed of light in vacuum), and $E_{\text{iso},II} = 4.94 \times 10^{-21} \text{ J} = 248 \text{ cm}^{-1} \times hc_0$.

The time constants of $\text{Ret}_{580,I}$ isomerization to Ret_{500} , $\tau_{\text{Ret}_{580,I}}$, of $\text{Ret}_{580,II}$ isomerization to Ret_{640} , $\tau_{\text{Ret}_{580,II}}$, of Ret_{500} deprotonation to Ret_{400} , $\tau_{PT,I}$, and of Ret_{640} deprotonation to Ret_{350} , $\tau_{PT,II}$, were determined above (Equations (3) and (4)). They are related to the energy activation barriers $E_{\text{act},I}$, $E_{\text{act},II}$, $E_{\text{act},PT,I}$, and $E_{\text{act},PT,II}$ by the Arrhenius relation [73] according to:

$$\tau_{\text{Ret}_{580,I}} = \tau_0 \exp\left(\frac{E_{\text{act},I}}{k_B\vartheta}\right) \quad (12)$$

$$\tau_{\text{Ret}_{580,II}} = \tau_0 \exp\left(\frac{E_{\text{act},II}}{k_B\vartheta}\right) \quad (13)$$

$$\tau_{PT,i} = \tau_0 \exp\left(\frac{E_{\text{act},PT,i}}{k_B\vartheta}\right), \quad i = I, II \quad (14)$$

where $\tau_0 = h/(k_B\vartheta)$ is the attempt time constant of barrier crossing [59,74]. Solving Equations (12)–(14) for the activation energy barriers gives:

$$E_{\text{act},I} = \ln\left(\frac{\tau_{\text{Ret}_{580,I}}}{\tau_0}\right)k_B\vartheta \quad (15)$$

$$E_{\text{act},II} = \ln\left(\frac{\tau_{\text{Ret}_{580,II}}}{\tau_0}\right)k_B\vartheta \quad (16)$$

$$E_{\text{act},PT,i} = \ln\left(\frac{\tau_{PT,i}}{\tau_0}\right)k_B\vartheta, \quad i = I, II \quad (17)$$

Insertion of parameters ($\vartheta = 296 \text{ K}$, $\tau_0 \approx 1.6 \times 10^{-13} \text{ s}$, $\tau_{\text{Ret}_{580,I}} = 3.8 \text{ d}$, $\tau_{\text{Ret}_{580,II}} = 120 \text{ d}$, $\tau_{PT,I} \approx \tau_{PT,II} \approx 42 \text{ d}$) leads to $E_{\text{act},I} = 1.72 \times 10^{-19} \text{ J} = 8670 \text{ cm}^{-1} \times hc_0$, $E_{\text{act},II} = 1.86 \times 10^{-19} \text{ J} = 9380 \text{ cm}^{-1} \times hc_0$, and $E_{\text{act},PT,I} \approx E_{\text{act},PT,II} \approx 1.82 \times 10^{-19} \text{ J} \approx 9160 \text{ cm}^{-1} \times hc_0$.

The performed data analysis of fresh thawed and of heat treated QuasAr1 allowed to determine the absorption cross-section spectra of PRSB Ret_{580} (a composition of PRSB 13-*cis* isomer $\text{Ret}_{580,I}$ and PRSB all-*trans* isomer $\text{Ret}_{580,II}$ in two different protein adjacent amino acid arrangements Apoprotein_{initial,I} and Apoprotein_{initial,II}) and of the RSB Ret_{380} (likely unresolved composition of Ret_{350} and Ret_{400}) which are shown in Figure S3. Knowledge of the absorption cross-section spectra

allowed the determination of the radiative lifetimes τ_{rad} of the S_1 – S_0 emission transitions using the Strickler–Berg formula according to [75–77]:

$$\tau_{rad} = \frac{n_A \bar{\lambda}_F^{-3}}{8\pi c_0 n_F^3 \bar{\sigma}} \quad (18)$$

where n_A and n_F are the average refractive indices of the aqueous buffer solution in the S_0 – S_1 absorption band region and the S_1 – S_0 emission band region, respectively, and c_0 is the velocity of light in vacuum. $\bar{\lambda}_F = \left(\int_{em} E_F(\lambda) \lambda^3 d\lambda / \int_{em} E_F(\lambda) d\lambda \right)^{1/3}$ is the average S_1 – S_0 fluorescence emission wavelength, and $\bar{\sigma}_a = \int_{abs} (\sigma_a(\lambda) / \lambda) d\lambda$ is the absorption cross-section strength of the S_0 – S_1 absorption band. Using appropriate absorption cross-section data from Figure S3, fluorescence quantum distribution data from Figure 6 and refractive indices of water, we determine $\tau_{rad}(\text{Ret}_{580}) = 9.32$ ns ($n_F = 1.33$, $n_A = 1.3328$, $\bar{\lambda}_F = 745$ nm, $\bar{\sigma}_a = 3.33 \times 10^{-17}$ cm²) and $\tau_{rad}(\text{Ret}_{380}) \approx 3.74$ ns ($n_F = 1.3366$, $n_A = 1.3406$, $\bar{\lambda}_F \approx 460$ nm, $\bar{\sigma}_a = 1.94 \times 10^{-17}$ cm²).

Average Strickler-Berg based fluorescence lifetimes $\tau_{F,SB}$ are obtained from the radiative lifetimes and the fluorescence quantum yields according to:

$$\tau_{F,SB} = \phi_F \tau_{rad} \quad (19)$$

The obtained values are $\tau_{F,SB}(\text{Ret}_{580}) \approx 61.5$ ps ($\phi_F \approx 0.0065$) and $\tau_{F,SB}(\text{Ret}_{380}) \approx 150$ ps ($\phi_F \approx 0.04$).

The fluorescence quantum yields and the fluorescence lifetimes of the protonated retinal Schiff base chromophore Ret_580 of fresh thawed QuasAr1 and of the thermally formed deprotonated retinal Schiff base Ret_380 are extraordinary large compared to the parent wild-type Archaeorhodopsin 3 ($\phi_F(\text{Arch}) = 9 \times 10^{-4}$) [36,42]. The performed mutations on Arch to get QuasAr1 led to a slowing down of the excited-state isomerization dynamics via twisted internal conversion (S_1 – S_0 conical intersection). They cause some restriction (barrier) along the reactive coordinate (twist angle) of photoisomerization. The slower relaxation along the S_1 state potential energy surface towards the funnel position of S_1 to S_0 internal conversion leads to the broad-band fluorescence emission of increased efficiency and longer fluorescence lifetime ([51] and references therein). In Table S1 of the Supplementary Materials (section S9) absorption, fluorescence, and primary photoisomerization parameters of some rhodopsins are collected for comparison.

4. Materials and Methods

4.1. Sample Preparation

QuasAr1 gene was a gift from Adam E. Cohen (Addgene plasmid # 64135, [42]). *E. coli* optimized gene was cloned into pET21a(+) vector between the NdeI and SalI restriction sites with a C-terminal TEV protease cleavage site and a HIS₆ tag (ENLYFQSLVDLEHHHHHH).

The expression plasmid (pet21a+) carrying QuasAr1 was transformed into C41(DE3) *E. coli* cells. To induce the protein expression we used 0.5 mM isopropyl β -D-thiogalactopyranoside (IPTG; Carl Roth GmbH, Karlsruhe, Germany) and the LB media was supplemented with 5 μ M all-trans retinal (ATR; Sigma-Aldrich, St. Louis, USA). The cells were incubated at 37 °C for 4 h and then harvested. The cells were disrupted using an EmulsiFlex-C3 Homogenizer (AVESTIN Inc., Ottawa, Canada). The membrane fraction was collected by ultracentrifugation (45,000 rpm) for 1 h at 4 °C (Type 45 Ti; Beckman Inc., Indianapolis, USA) and then resuspended in buffer containing 50 mM Tris-HCl (pH 8.0), 300 mM NaCl, 0.1 mM phenylmethanesulfonyl fluoride (PMSF), 1.5% n-dodecyl- β -D-maltoside (DDM, GLYCON Biochemicals GmbH, Luckenwalde, Germany), and 0.3% cholesteryl hemisuccinate (CHS, Sigma-Aldrich, St. Louis, USA) and stirred overnight for solubilization. The insoluble fraction was removed by ultracentrifugation (200,000 \times g, 1 h at 4 °C). The QuasAr1 protein was purified by Ni-NTA affinity and using an ÄKTAexpress protein purification system (GE Healthcare Life Science,

Chicago, USA) configured with a HisTrap HP Ni-NTA column. The protein was collected in the final buffer containing 50 mM Tris-HCl (pH 8.0), 150 mM NaCl, 0.02% DDM, 0.004% CHS, 0.1 mM PMSF, and 5% glycerol.

The expressed QuasAr1 protein in the final buffer was aliquoted to amounts of 30 μ L in Eppendorf tubes, shock-frozen, and stored at -80 °C until thawing for experimental investigations.

4.2. Spectroscopic Measurements

Transmission measurements, $T(\lambda)$ (λ is wavelength), were carried out with a spectrophotometer (Cary 50, Varian Australia Pty Ltd, Mulgrave, Victoria, Australia). Attenuation coefficient spectra were calculated by the relation, $\alpha(\lambda) = -\ln[T(\lambda)]/l$, where l is the sample length. In the case of negligible protein light scattering the attenuation coefficient spectrum $\alpha(\lambda)$ is equal to the absorption coefficient spectrum $\alpha_a(\lambda)$. Otherwise it comprises absorption (α_a) and scattering (α_s) contributions according to $\alpha(\lambda) = \alpha_a(\lambda) + \alpha_s(\lambda)$. The scattering coefficient spectrum is approximated by the empirical relation [78] $\alpha_s(\lambda) = \alpha_s(\lambda_0)(\lambda_0/\lambda)^\gamma$ where the wavelength λ_0 is selected in the transparency region and $\gamma \leq 4$ is fitted to the experimental attenuation in the transparency region. Absorption coefficient spectra became available by subtracting the scattering contribution from the measured attenuation coefficient spectra.

The QuasAr1 melting was studied by stepwise sample heating up, then cooling down and thereby measuring the attenuation coefficient spectra development [58,59]. The apparent protein melting temperature ϑ_m was derived from the onset of strong light attenuation in the transparency region of QuasAr1.

The thermal stability of QuasAr1 at room temperature (21–25 °C) and refrigerator temperature (2.5 ± 0.5 °C) was determined by storing QuasAr1 samples at these temperatures in the dark and measuring transmission spectra at certain time intervals.

Fluorescence spectroscopic measurements were carried out with a spectrofluorimeter (Cary Eclipse, Varian Australia Pty Ltd, Mulgrave, Victoria, Australia). Fluorescence emission quantum distributions $E_F(\lambda)$ were determined from fluorescence emission spectra measurements at fixed excitation wavelengths [52,79,80]. The dye rhodamine 6G in methanol was used as reference standard for fluorescence quantum distribution calibration (fluorescence quantum yield $\phi_{F,ref} = 0.93$ [81]). The fluorescence quantum yield ϕ_F was calculated using the relation $\phi_F = \int_{em} E_F(\lambda)d\lambda$ where the integration runs over the fluorescence emission wavelength region. Fluorescence excitation quantum distributions $E_{ex}(\lambda)$ were recorded by scanning the fluorescence excitation wavelength over the absorption wavelength region at fixed fluorescence detection wavelengths [82]. Magic angle conditions were applied for the fluorescence recordings (vertical polarized excitation and orientation of the fluorescence detection polarizer at an angle of 54.7° to the vertical [83]). The spectra were corrected for the spectral sensitivity of the spectrometer and the photodetector.

5. Conclusions

The rhodopsin fluorescent voltage sensor QuasAr1 [42] was characterized by its absorption and emission spectroscopic behavior and its long-time thermal stability. At refrigerator temperature it may be used over a period of about 40 days without significant absorption and fluorescence spectroscopic changes. At room temperature it is possible to store the voltage sensor over about one day without severe retinal Schiff base deprotonation and opsin protein restructuring.

In the dark at room temperature the formation of new retinal isomers in the ground-state of QuasAr1 took place by thermal overcoming of energy barriers and by lowering the potential energy levels of the protonated Schiff base isomers (dominantly Ret_500 and Ret_640) and the deprotonated Schiff base isomers (dominantly Ret_400 and Ret_350) due to dynamic protein restructuring on a time scale of days. The isomerization dynamics of QuasAr1 retinals in the excited state (photoisomerization) occurs on a ten picosecond timescale due to a different barrier-involved S_1 state potential energy surface structure.

Supplementary Materials: Supplementary Materials can be found at <http://www.mdpi.com/1422-0067/20/17/4086/s1>. References [84–103] are cited in the supplementary materials

Author Contributions: The study was initiated by A.S. and P.H. who expressed, purified and delivered the protein. A.P. carried out the absorption and emission spectroscopic measurements. The manuscript was written by A.P. and commented and improved by A.S. and P.H.

Funding: This research received no external funding.

Acknowledgments: Alfons Penzkofer thanks Franz J. Gießibl, University of Regensburg, for his kind hospitality. The work was supported by the European Research Council (ERC, MERA project), the DFG Cluster of Excellence ‘Unifying Systems in Catalysis’ EXC314, and the Gottfried Wilhelm Leibniz Prize to Peter Hegemann and Arita Silapetere. Peter Hegemann is a Hertie Professor for Neuroscience and supported by the Hertie-Foundation.

Conflicts of Interest: The authors declare no conflict of interest.

Abbreviations

Arch	Archaerhodopsin 3 from <i>Halorubrum sodomense</i>
GECI	Genetically encoded calcium indicator
GEVI	Genetically encoded voltage indicator
PRSB	Protonated retinal Schiff base
QuasAr	Quality superior to Arch
Ret_xxx	Retinal with absorption maximum approximately at xxx nm
RSB	Retinal Schiff base
Trp	Tryptophan
Tyr	Tyrosine
VSD	Voltage sensing domain

References

1. Ainsworth, M.; Lee, S.; Cunningham, M.O.; Traub, R.D.; Kopell, N.J.; Whittington, M.A. Rates and rhythms: A synergistic view of frequency and temporal coding in neural networks. *Neuron* **2012**, *75*, 572–583. [[CrossRef](#)] [[PubMed](#)]
2. Antic, S.D.; Empson, R.M.; Knöpfel, T. Voltage imaging to understand brain connections and neural function. *J. Neurophysiol.* **2016**, *116*, 135–152. [[CrossRef](#)]
3. Wilson, J.R.; Clark, R.B.; Banderali, U.; Giles, W.R. Measurement of the membrane potential in small cells using patch clamp methods. *Channels* **2011**, *5*, 530–537. [[CrossRef](#)] [[PubMed](#)]
4. Shoham, D.; Glaser, D.E.; Arieli, A.; Kenet, T.; Wijnbergen, C.; Toledo, Y.; Hildesheim, R.; Grinvald, A. Imaging cortical dynamics at high spatial and temporal resolution with novel blue voltage-sensitive dyes. *Neuron* **1999**, *24*, 791–802. [[CrossRef](#)]
5. Kee, M.Z.; Wuskell, J.P.; Loew, L.M.; Augustine, G.J.; Sekino, Y. Imaging activity of neuronal populations with new long-wavelength voltage-sensitive dyes. *Brain Cell Biol.* **2008**, *36*, 157–172. [[CrossRef](#)] [[PubMed](#)]
6. Miller, E.W.; Lin, J.Y.; Frady, E.P.; Stinbach, P.A.; Kristan, W.B.; Tsien, R.Y. Optically monitoring voltage in neurons by photo-induced electron transfer through molecular wires. *PNAS* **2012**, *109*, 2114–2119. [[CrossRef](#)]
7. Tsytsarev, V.; Liao, L.D.; Kong, K.V.; Liu, Y.H.; Erzurumlu, R.S.; Olivo, M.; Nitish, N.V. Recent progress in voltage-sensitive dye imaging for neuroscience. *J. Nanosci. Nanotechnol.* **2014**, *14*, 4733–4744. [[CrossRef](#)] [[PubMed](#)]
8. Ortiz, G.; Liu, P.; Naing, S.H.H.; Muller, V.R.; Miller, E.W. Synthesis of sulfonated carbofluoresceins for voltage imaging. *J. Am. Chem. Soc.* **2019**, *141*, 6631–6638. [[CrossRef](#)] [[PubMed](#)]
9. Mank, M.; Griesbeck, O. Genetically encoded calcium indicators. *Chem.Rev.* **2008**, *108*, 1550–1564. [[CrossRef](#)]
10. Akerboom, J.; Calderón, N.C.; Tian, L.; Wabnig, S.; Prigge, M.; Tolö, J.; Gordus, A.; Orger, M.B.; Severi, K.E.; Macklin, J.J.; et al. Genetically encoded calcium indicators for multi-color neural activity imaging and combination with optogenetics. *Front. Mol. Neurosci.* **2013**, *6*, 1–29. [[CrossRef](#)]
11. Barykina, N.V.; Subach, O.M.; Piatkevich, K.D.; Jung, E.E.; Malyshev, A.Y.; Smirnov, I.V.; Bogorodskiy, A.O.; Borshchevskiy, V.I.; Varizhuk, A.M.; Pozmogova, G.E.; et al. Green fluorescent genetically encoded calcium indicator based on calmodulin/M13-peptide from fungi. *PLoS ONE* **2017**, *12*, e0183757. [[CrossRef](#)] [[PubMed](#)]

12. Looger, L.L.; Griesbeck, O. Genetically encoded neural activity indicators. *Curr. Opin. Neurobiol.* **2012**, *22*, 18–23. [[CrossRef](#)] [[PubMed](#)]
13. Broussard, G.J.; Liang, R.; Tian, L. Monitoring activity in neural circuits with genetically encoded indicators. *Front. Mol. Neurosci.* **2014**, *7*, 97. [[CrossRef](#)] [[PubMed](#)]
14. Nguyen, C.; Upadhyay, H.; Murphy, M.; Borja, G.; Rozsahegyi, E.M.; Barnett, A.; Brookings, T.; McManus, O.B.; Werley, C.A. Simultaneous voltage and calcium imaging and optogenetic stimulation with high sensitivity and a wide field of view. *Biomed. Opt. Express* **2019**, *10*, 789–806. [[CrossRef](#)] [[PubMed](#)]
15. Mutoh, H.; Akemann, W.; Knöpfel, T. Genetically engineered fluorescent voltage reporters. *ACS Chem. Neurosci.* **2012**, *3*, 585–592. [[CrossRef](#)] [[PubMed](#)]
16. Gong, Y. The evolving capabilities of rhodopsin-based genetically encoded voltage indicators. *Curr. Opin. Chem. Biol.* **2015**, *27*, 84–89. [[CrossRef](#)] [[PubMed](#)]
17. Yang, H.H.; St-Pierre, F. Genetically encoded voltage indicators: Opportunities and challenges. *J. Neurosci.* **2016**, *36*, 9977–9989. [[CrossRef](#)] [[PubMed](#)]
18. Nakajima, R.; Jung, A.; Yoon, B.J.; Baker, B.J. Optogenetic monitoring of synaptic activity with genetically encoded voltage indicators. *Front. Synaptic Neurosci.* **2016**, *8*, 1–9. [[CrossRef](#)]
19. St-Pierre, F.; Chavarha, M.; Lin, M.Z. Design and sensing mechanisms of genetically encoded fluorescent voltage indicators. *Curr. Opin. Chem. Biol.* **2015**, *27*, 31–38. [[CrossRef](#)]
20. Xu, Y.; Zou, P.; Cohen, A.E. Voltage imaging with genetically encoded indicators. *Curr. Opin. Chem. Biol.* **2017**, *39*, 1–10. [[CrossRef](#)]
21. Zhang, H.; Reichert, E.; Cohen, A.E. Optical electrophysiology for probing function and pharmacology of voltage-gated ion channels. *eLife* **2016**, *5*, e15202. [[CrossRef](#)] [[PubMed](#)]
22. Adam, Y.; Kim, J.J.; Lou, S.; Zhao, Y.; Brinks, D.; Wu, H.; Mostajo-Radji, M.A.; Kheifets, S.; Parot, V.; Chettih, S.; et al. All-optical electrophysiology reveals brain-state dependent changes in hippocampal subthreshold dynamics and excitability. *bioRxiv preprint* **2018**. [[CrossRef](#)]
23. Lin, M.Z.; Schnitzer, M.J. Genetically encoded indicators of neuronal activity. *Nat. Neurosci.* **2016**, *19*, 1142–1153. [[CrossRef](#)] [[PubMed](#)]
24. Knöpfel, T.; Gallero-Salas, Y.; Song, C. Genetically encoded voltage indicators for large scale cortical imaging come of age. *Curr. Opin. Chem. Biol.* **2015**, *27*, 75–83. [[CrossRef](#)] [[PubMed](#)]
25. Inagaki, I.; Nagai, T. Current progress in genetically encoded voltage indicators for neural activity recording. *Curr. Opin. Chem. Biol.* **2016**, *33*, 95–100. [[CrossRef](#)] [[PubMed](#)]
26. Storaice, D.; Rad, M.S.; Kang, B.; Cohen, L.B.; Hughes, T.; Baker, B.J. Towards better genetically encoded sensors of membrane potential. *Trends Neurosci.* **2016**, *39*, 277–289. [[CrossRef](#)] [[PubMed](#)]
27. Bando, Y.; Sakamoto, M.; Kim, S.; Ayzenshtat, I.; Yuste, R. Comparative evaluation of genetically encoded voltage indicators. *Cell Rep.* **2019**, *26*, 802–813. [[CrossRef](#)] [[PubMed](#)]
28. Adam, Y.; Kim, J.J.; Lou, S.; Zhao, Y.; Xie, M.E.; Brinks, D.; Wu, H.; Mostajo-Radji, M.A.; Kheifets, S.; Parot, V.; et al. Voltage imaging and optogenetics reveal behaviour-dependent changes in hippocampal dynamics. *Nature* **2019**, *569*, 413–417. [[CrossRef](#)] [[PubMed](#)]
29. St-Pierre, F.; Marshall, J.D.; Yang, Y.; Gong, Y.; Schnitzer, M.J.; Lin, M.Z. High fidelity optical reporting of neural electrical activity with an ultrafast fluorescent voltage sensor. *Nat. Neurosci.* **2014**, *17*, 884–889. [[CrossRef](#)]
30. Dimitrov, D.; He, Y.; Mutoh, V.; Baker, B.J.; Cohen, L.; Akemann, W.; Knöpfel, T. Engineering and characterization of an enhanced fluorescent protein voltage sensor. *PLoS ONE* **2007**, *2*, e440. [[CrossRef](#)]
31. Mishina, Y.; Mutoh, H.; Knöpfel, T. Transfer of Kv3.1 voltage sensor features to the isolated Ci-VSP voltage-sensing domain. *Biophys. J.* **2012**, *103*, 669–676. [[CrossRef](#)] [[PubMed](#)]
32. Jin, L.; Han, Z.; Woollorton, J.R.; Cohen, L.B.; Pieribone, V.A. Single action potentials and subthreshold electrical events imaged in neurons with a fluorescent protein voltage probe. *Neuron* **2012**, *75*, 779–785. [[CrossRef](#)] [[PubMed](#)]
33. Sung, U.; Sepeshri-Rad, M.; Piao, H.H.; Jin, L.; Huges, T.; Cohen, L.J.; Baker, L.B. Developing fast fluorescent protein voltage sensors by optimizing FRET interactions. *PLoS ONE* **2015**, *10*, e0141585. [[CrossRef](#)] [[PubMed](#)]

34. Kost, L.A.; Nikitin, E.S.; Ivanova, V.O.; Sung, U.; Putintseva, E.V.; Chudakov, D.M.; Balaban, P.M.; Lukyanov, K.A. Insertion of the voltage-sensitive domain into circularly permuted red fluorescent protein as a design for genetically encoded voltage sensor. *PLoS ONE* **2017**, *12*, e0184225. [[CrossRef](#)] [[PubMed](#)]
35. Kralj, J.M.; Hochbaum, D.R.; Douglass, A.D.; Cohen, A.E. Electrical spiking in *Escherichia coli* probed with a fluorescent voltage-indicating protein. *Science* **2011**, *333*, 345–348. [[CrossRef](#)] [[PubMed](#)]
36. Kralj, J.M.; Douglass, A.D.; Hochbaum, D.R.; Maclaurin, D.; Cohen, A.E. Optical recording of action potentials in mammalian neurons using microbial rhodopsin. *Nat. Meth.* **2012**, *9*, 90–95. [[CrossRef](#)]
37. Venkatachalam, V.; Brinks, D.; Maclaurin, D.; Hochbaum, D.R.; Kralj, J.M.; Cohen, A.E. Flash memory: Photochemical imprinting of neuronal action potentials onto a microbial rhodopsin. *J. Am. Chem. Soc.* **2014**, *136*, 2529–2537. [[CrossRef](#)] [[PubMed](#)]
38. Maclaurin, D.; Venkatachalam, V.; Lee, H.; Cohen, A.E. Mechanism of voltage-sensitive fluorescence in a microbial rhodopsin. *PNAS* **2013**, *110*, 5939–5944. [[CrossRef](#)]
39. Govindjee, R.; Becher, B.; Ebrey, T.G. The fluorescence from the chromophore of the purple membrane protein. *Biophys. J.* **1978**, *22*, 67–77. [[CrossRef](#)]
40. Kochendoerfer, G.G.; Mathies, R.A. Spontaneous emission study of the femtosecond isomerization dynamics of rhodopsin. *J. Phys. Chem.* **1996**, *100*, 14526–14532. [[CrossRef](#)]
41. Lenz, M.O.; Huber, R.; Schmidt, B.; Gilch, P.; Kalmbach, R.; Engelhard, M.; Wachtveitl, J. First steps of retinal photoisomerization in proteorhodopsin. *Biophys. J.* **2006**, *91*, 255–262. [[CrossRef](#)] [[PubMed](#)]
42. Hochbaum, D.R.; Zhao, Y.; Farhi, S.L.; Klapoetke, N.; Werley, C.A.; Kapoor, V.; Zou, P.; Kralj, J.M.; Maclaurin, D.; Smedemark-Margulies, N.; et al. All-optical electrophysiology in mammalian neurons using engineered microbial rhodopsins. *Nat. Meth.* **2014**, *11*, 825–833. [[CrossRef](#)] [[PubMed](#)]
43. McIsaac, R.S.; Engqvist, M.K.M.; Wannier, T.; Rosenthal, A.Z.; Herwig, L.; Flytzanis, N.C.; Imasheva, E.S.; Lanyi, J.K.; Balashov, S.P.; Gradinaru, V. Directed evolution of a far-red fluorescent rhodopsin. *PNAS* **2014**, *111*, 13034–13039. [[CrossRef](#)] [[PubMed](#)]
44. Engqvist, M.K.M.; McIsaac, R.S.; Dollinger, P.; Flytzanis, N.C.; Abrams, M.; Schor, S.; Arnold, F.H. Directed evolution of *Gloeobacter violaceus* rhodopsin spectral properties. *J. Mol. Biol.* **2015**, *427*, 205–220. [[CrossRef](#)] [[PubMed](#)]
45. Chien, M.P.; Brinks, D.; Adam, Y.; Bloxham, W.; Kheifets, S.; Cohen, A.E. Two-photon photoactivated voltage imaging in tissue with an Archaerhodopsin-derived reporter. *bioRxiv preprint* **2017**. [[CrossRef](#)]
46. Gong, Y.; Li, J.Z.; Schnitzer, M.J. Enhanced Archaerhodopsin fluorescent protein voltage indicators. *PLoS ONE* **2013**, *8*, e66959. [[CrossRef](#)] [[PubMed](#)]
47. Flytzanis, N.C.; Bedbrook, C.N.; Engqvist, M.K.M.; Xiao, C.; Chan, K.Y.; Sternberg, P.W.; Arnold, F.H.; Gradinaru, V. Archaerhodopsin variants with enhanced voltage-sensitive fluorescence in mammalian and *Caenorhabditis elegans* neurons. *Nat. Commun.* **2014**, *5*, 4894. [[CrossRef](#)] [[PubMed](#)]
48. Piatkevich, K.D.; Jung, E.E.; Straub, C.; Linghu, C.; Park, D.; Suk, H.J.; Hochbaum, D.R.; Goodwin, D.; Pnevmatikakis, E.; Pak, N.; et al. A robotic multidimensional directed evolution approach applied to fluorescent voltage reporters. *Nat. Chem. Biol.* **2018**, *14*, 352–360. [[CrossRef](#)] [[PubMed](#)]
49. Zou, P.; Zhao, Y.; Douglass, A.D.; Hochbaum, D.R.; Brinks, D.; Werley, C.A.; Harrison, D.J.; Campbell, R.E.; Cohen, A.E. Bright and fast multicoloured voltage reporters via electrochromic FRET. *Nat. Commun.* **2014**, *5*, 4625. [[CrossRef](#)]
50. Gong, Y.; Wagner, M.J.; Li, Z.; Schnitzer, M.J. Imaging neural spiking in brain tissue using FRET-opsin protein voltage sensors. *Nat. Commun.* **2014**, *5*, 3674. [[CrossRef](#)]
51. Penzkofer, A.; Hegemann, P.; Kateriya, S. Organic dyes in optogenetics. In *Organic Lasers and Organic Photonics*; Duarte, F.J., Ed.; IOP Publishing: Bristol, UK, 2018; pp. 13-1–13-114.
52. Förster, T. *Fluoreszenz organischer Verbindungen*; Vandenhoeck und Ruprecht: Göttingen: Lower Saxony, Germany, 1951; pp. 83–86.
53. Valeur, B.; Berberan-Santos, M.N. *Molecular Fluorescence: Principles and Applications*, 2nd ed.; Wiley-VCH: Weinheim, Baden-Württemberg, Germany, 2012; pp. 213–261.
54. Penzkofer, A.; Luck, M.; Mathes, T.; Hegemann, P. Bistable retinal Schiff base photodynamics of histidine kinase rhodopsin HKR1 from *Chlamydomonas reinhardtii*. *Photochem. Photobiol.* **2014**, *90*, 773–785. [[PubMed](#)]

55. Chen, R.F. Fluorescence quantum yields of tryptophan and tyrosine. *Anal. Lett.* **1967**, *1*, 35–42. [[CrossRef](#)]
56. Eisinger, J.; Navon, G. Fluorescence quenching and isotope effect of tryptophan. *J. Chem. Phys.* **1969**, *50*, 2069–2077. [[CrossRef](#)] [[PubMed](#)]
57. Kirby, E.P.; Steiner, R.F. The influence of solvent and temperature upon the fluorescence of indole derivatives. *J. Phys. Chem.* **1970**, *74*, 4480–4490. [[CrossRef](#)]
58. Penzkofer, A.; Scheib, U.; Hegemann, P.; Stehfest, K. Absorption and emission spectroscopic investigation of thermal dynamics and photo-dynamics of the rhodopsin domain of the rhodopsin-guanylyl cyclase from the aquatic fungus *Blastocladiella emersonii*. *BAOJ Phys.* **2016**, *2*, 006.
59. Penzkofer, A.; Stierl, M.; Hegemann, P.; Kateriya, S. Thermal protein unfolding in photo-activated adenylate cyclase nano-clusters from the amoeboid flagellate *Naegleria gruberi* NEG-M strain. *J. Photochem. Photobiol. A: Chem.* **2011**, *225*, 42–51. [[CrossRef](#)]
60. Lu, Y.; Penzkofer, A. Absorption behaviour of methanolic rhodamine 6G solutions at high concentration. *Chem. Phys.* **1986**, *107*, 175–184. [[CrossRef](#)]
61. Penzkofer, A.; Leupacher, W.; Meier, B.; Runde, B.; Drexhage, K.H. Concentration dependent absorption and emission behaviour of a pyrimidonecarbocyanine dye in hexafluoroisopropanol. *Chem. Phys.* **1987**, *115*, 143–150. [[CrossRef](#)]
62. Penzkofer, A.; Leupacher, W. S₀-S₁ two photon absorption dynamics of organic dye solutions. *Opt. Quant. Electron.* **1987**, *19*, 327–349. [[CrossRef](#)]
63. Weigand, R.; Rotermund, F.; Penzkofer, A. Aggregation dependent absorption reduction of indocyanine green. *J. Phys. Chem. A* **1997**, *101*, 7729–7734. [[CrossRef](#)]
64. Malencik, D.A.; Sprouse, J.F.; Swanson, C.A.; Anderson, S.R. Dityrosine: Preparation, isolation, and analysis. *Analyt. Biochem.* **1996**, *242*, 202–213. [[CrossRef](#)] [[PubMed](#)]
65. Bent, D.V.; Hayon, E. Excited state chemistry of aromatic amino acids and related peptides. I. Tyrosine. *J. Am. Chem. Soc.* **1975**, *97*, 2599–2606. [[CrossRef](#)] [[PubMed](#)]
66. Jovanovic, S.V.; Simic, M.G. Repair of tryptophan radicals by antioxidants. *J. Free Rad. Biol. Med.* **1985**, *1*, 125–129. [[CrossRef](#)]
67. Penzkofer, A.; Tanwar, M.; Veetil, S.K.; Kateriya, S.; Stierl, M.; Hegemann, P. Photo-dynamics of the lyophilized photo-activated adenylate cyclase NgPAC2 from the amoeboid flagellate *Naegleria gruberi* NEG-M strain. *Chem. Phys.* **2013**, *423*, 192–201. [[CrossRef](#)]
68. Rizzini, L.; Favory, J.J.; Cloix, C.; Faggionato, D.; O'Hara, A.; Kaiserli, E.; Baumeister, R.; Schäfer, E.; Nagy, F.; Jenkins, G.I.; et al. Perception of UV-B by the *Arabidopsis* UVR8 protein. *Science* **2011**, *332*, 1103–1106. [[CrossRef](#)] [[PubMed](#)]
69. Christie, J.M.; Arvai, A.S.; Baxter, K.J.; Heilmann, M.; Pratt, A.J.; O'Hara, A.; Kelly, S.M.; Hothorn, M.; Smith, B.O.; Hitomi, K.; et al. Plant UVR8 photoreceptor senses UV-B by tryptophan-mediated disruption of cross-dimer salt bridges. *Science* **2012**, *335*, 1492–1496. [[CrossRef](#)] [[PubMed](#)]
70. Liu, J.; Ward, A.; Gao, J.; Dong, Y.; Nishio, N.; Inada, H.; Kang, L.; Yu, Y.; Ma, D.; Xu, T.; et al. *C. elegans* phototransduction requires a G protein-dependent cGMP pathway and a taste receptor homolog. *Nat. Neurosci.* **2010**, *13*, 715–722. [[CrossRef](#)] [[PubMed](#)]
71. Gong, J.; Yuan, Y.; Ward, A.; Kang, L.; Zhang, B.; Wu, Z.; Peng, J.; Feng, V.; Liu, J.; Xu, X.Z.S. The *C. elegans* taste receptor homolog LITE-1 is a photoreceptor. *Cell* **2016**, *167*, 1252–1263. [[CrossRef](#)]
72. Bäumler, W.; Penzkofer, A. Isomerization of DODCI in the S₀ ground state. *Chem. Phys. Lett.* **1988**, *150*, 315–320. [[CrossRef](#)]
73. Fleming, G.R. *Chemical Applications in Ultrafast Spectroscopy*; Oxford University Press: New York, NY, USA, 1986; pp. 179–195.
74. Voet, D.; Voet, J.G. *Biochemistry*, 4th ed.; John Wiley & Sons: Hoboken, NJ, USA, 2004; pp. 482–505.
75. Strickler, S.J.; Berg, R.A. Relationship between absorption intensity and fluorescence lifetime of molecules. *J. Chem. Phys.* **1962**, *37*, 814–822. [[CrossRef](#)]
76. Birks, J.B.; Dyson, D.J. The relations between the fluorescence and absorption properties of organic molecules. *Proc. Roy. Soc. London Ser. A* **1963**, *275*, 135–148.
77. Deshpande, A.V.; Beidoun, A.; Penzkofer, A.; Wagenblast, G. Absorption and emission spectroscopic investigation of cyanovinyl-diethylaniline dye vapors. *Chem. Phys.* **1990**, *142*, 123–131. [[CrossRef](#)]
78. Penzkofer, A.; Shirdel, J.; Zirak, P.; Breitkreuz, H.; Wolf, E. Protein aggregation studied by forward light scattering and transmission analysis. *Chem. Phys.* **2007**, *342*, 55–63. [[CrossRef](#)]

79. Holzer, W.; Pichlmaier, M.; Penzkofer, A.; Bradley, D.D.C.; Blau, W.J. Fluorescence spectroscopic behavior of neat and blended polymer thin films. *Chem. Phys.* **1999**, *246*, 445–462. [[CrossRef](#)]
80. Penzkofer, A. Photoluminescence behavior of riboflavin and lumiflavin in liquid solutions and solid films. *Chem. Phys.* **2012**, *400*, 142–153. [[CrossRef](#)]
81. Madge, D.; Wong, R.; Seybold, P.G. Fluorescence quantum yields and their relation to lifetimes of rhodamine 6G and fluorescein in nine solvents: Improved absolute standards for quantum yields. *Photochem. Photobiol.* **2002**, *75*, 327–334.
82. Birkmann, C.; Penzkofer, A.; Tsuboi, T. Fluorescence excitation spectroscopic characterization of colour centres in a LiF crystal. *Appl. Phys. B* **2003**, *77*, 625–632. [[CrossRef](#)]
83. Dörr, F. Spectroscopy with polarized light. *Angew. Chem. Int. Ed.* **1966**, *5*, 478–495. [[CrossRef](#)]
84. Lindsey, J. PhotochemCAD Spectra by Category. Available online: <https://omlc.org/spectra/PhotochemCAD/html/> (accessed on 7 July 2019).
85. Tsuboi, T.; Penzkofer, A.; Lammel, O. Oscillator strength of F₂⁻ colour centres in LiF crystal. *Opt. Quant. Electron.* **2003**, *35*, 267–274. [[CrossRef](#)]
86. Sineshchekov, V.A.; Balashov, S.P.; Litvin, F.F. Fluorescence of rhodopsin in the retinal rod outer segments of the frog at 77 K. *Dokl. AN SSSR* **1983**, *270*, 1231–1235.
87. Doukas, A.G.; Junnarker, M.R.; Alfano, R.R.; Callender, R.H.; Kakitani, T.; Honig, B. Fluorescence quantum yield of visual pigments: Evidence for subpicosecond isomerization rates. *PNAS* **1984**, *81*, 4790–4794. [[CrossRef](#)] [[PubMed](#)]
88. Kandori, H.; Shichida, Y.; Yoshizawa, T. Photoisomerization in rhodopsin. *Biochemistry (Moscow)* **2001**, *66*, 1197–1209. [[CrossRef](#)]
89. Ohtani, H.; Tsukamoto, Y.; Sakoda, Y.; Hamaguchi, H. Fluorescence spectra of bacteriorhodopsin and the intermediates O and Q at room temperature. *FEBS Lett.* **1995**, *359*, 65–68. [[CrossRef](#)]
90. Polland, H.J.; Zinth, W.; Kaiser, W. New investigations of the primary processes of bacteriorhodopsin and of halorhodopsin. *Ultrafast Phenomena IV, Springer Ser. Chem. Phys.* **1984**, *38*, 456–458.
91. Lutz, I.; Sieg, A.; Wegener, A.A.; Engelhard, M.; Boche, I.; Otsuka, M.; Oesterhelt, D.; Wachtveitl, J.; Zinth, W. Primary reactions of sensory rhodopsins. *PNAS* **2001**, *98*, 962–967. [[CrossRef](#)] [[PubMed](#)]
92. Dobler, J.; Zinth, W.; Kaiser, W.; Oesterhelt, D. Excited-state reaction dynamics of bacteriorhodopsin studied by femtosecond spectroscopy. *Chem. Phys. Lett.* **1988**, *144*, 215–220. [[CrossRef](#)]
93. Du, M.; Fleming, G.R. Femtosecond time-resolved fluorescence spectroscopy of bacteriorhodopsin: Direct observation of excited state dynamics in the primary step of the proton pump cycle. *Biophys. Chem.* **1993**, *48*, 101–111. [[CrossRef](#)]
94. Haake, S.; Schenkl, S.; Vinzani, S.; Chergui, M. Femtosecond and picosecond fluorescence of native bacteriorhodopsin and nonisomerizing analog. *Biopolymers (Biospectroscopy)* **2002**, *67*, 306–309. [[CrossRef](#)]
95. Peters, F.; Herbst, J.; Tittor, J.; Oesterhelt, D.; Diller, R. Primary reaction dynamics of halorhodopsin, observed by sub-picosecond IR – vibrational spectroscopy. *Chem. Phys.* **2009**, *323*, 109–116. [[CrossRef](#)]
96. Arlt, T.; Schmidt, S.; Zinth, W.; Haupt, U.; Oesterhelt, D. The initial reaction dynamics of the light-driven chloride pump halorhodopsin. *Chem. Phys. Lett.* **1995**, *241*, 559–565. [[CrossRef](#)]
97. Polland, H.J.; Franz, M.A.; Zinth, W.; Kaiser, W.; Hegemann, P.; Oesterhelt, D. Picosecond events in the photochemical cycle of the light-driven chloride-pump halorhodopsin. *Biophys. J.* **1985**, *47*, 55–59. [[CrossRef](#)]
98. Kandori, H.; Tomioka, H.; Sasabe, H. Excited-state dynamics of *Pharaonis* phoborhodopsin probed by femtosecond fluorescence spectroscopy. *J. Phys. Chem. A* **2002**, *106*, 2091–2095. [[CrossRef](#)]
99. Verhoeven, M.K.; Bamann, C.; Blöcher, R.; Förster, U.; Bamberg, E.; Wachtveitl, J. The photocycle of channelrhodopsin-2: Ultrafast reaction dynamics and subsequent reaction steps. *ChemPhysChem.* **2010**, *11*, 3113–3122. [[CrossRef](#)]
100. Wand, A.; Rozin, R.; Eliash, T.; Jung, K.H.; Sheves, M.; Ruhman, S. Asymmetric toggling of a natural photoswitch: Ultrafast spectroscopy of *Anabaena* sensory rhodopsin. *J. Am. Chem. Soc.* **2011**, *133*, 20922–20932. [[CrossRef](#)] [[PubMed](#)]
101. Luck, M.; Mathes, T.; Bruun, S.; Fudim, R.; Hagedorn, R.; Nguyen, T.M.T.; Kateriya, S.; Kennis, J.T.M.; Hildebrandt, P.; Hegemann, P. A photochromic histidine kinase rhodopsin (HKR1) that is bimodally switched by ultraviolet and blue light. *J. Biol. Chem.* **2012**, *287*, 40083–40090. [[CrossRef](#)]

102. Penzkofer, A.; Scheib, U.; Stehfest, K.; Hegemann, P. Absorption and emission spectroscopic investigation of thermal dynamics and photo-dynamics of the rhodopsin domain of the rhodopsin-guanylyl cyclase from the nematophagous fungus *Catenaria anguillulae*. *Int. J. Mol. Sci.* **2017**, *18*, 2099. [[CrossRef](#)] [[PubMed](#)]
103. Saint Clair, E.C.; Ogren, J.I.; Mamaev, S.; Russano, D.; Kralj, J.M.; Rothschild, J. Near-IR resonance Raman spectroscopy of Archaerhodopsin 3: Effects of transmembrane potential. *J. Phys. Chem. B* **2012**, *116*, 14592–14601. [[CrossRef](#)]



© 2019 by the authors. Licensee MDPI, Basel, Switzerland. This article is an open access article distributed under the terms and conditions of the Creative Commons Attribution (CC BY) license (<http://creativecommons.org/licenses/by/4.0/>).